Thermal and Mechanical Characterization of the TT Detector for the LHCb Experiment

---

Master Thesis

Physics Institute of the University of Zürich

Angela Büchler

Prof. Dr. Ulrich Straumann
PD Dr. Frank Lehner

February 2007

Contents

1 The TT-station as a part of the LHCb experiment 2
1.1 CP violation motivating the LHCb experiment 2
1.2 The LHCb detector and the Trigger Tracker station 2

2 Alignment of the TT Station at CERN 6
2.1 Experimental setup 6
2.2 Data reconstruction and results 9
2.2.1 Leveling 9
2.2.2 Alignment in x-direction 12
2.2.3 Alignment with the laser system 14

3 Thermal studies in the test box 16
3.1 Experimental setup in the assembly hall 36G38 16
3.2 Data reconstruction 18
3.3 Calibration 21
3.4 Pressure drop of the cooling plate 21
3.5 Temperature profile 24
3.5.1 Heating load measurements 25
3.5.2 U-value of the test box 27
3.5.3 Influence of the flow rate on the temperatures 30

4 Thermal characterization of the TT-station 32
4.1 Experimental setup 32
4.2 Data reconstruction 33
4.3 Calibration 33
4.4 Temperature profile for heating load measurements 35
4.5 U-value of the station box 35
4.6 Warm up measurement 37

5 Conclusions 40

6 Acknowledgments 41

References 42

A Alignment data tables 44

B Calibration data tables 49

C Results of the heating load measurements 51

D Measurement reports 55

Abstract

The goal of this thesis was the mechanical and thermal characterization of the LHCb Trigger-Tracker station (TT). The work was divided into two parts: the mechanical alignment of the detector's support structure (rails) and thermal studies leading to a detailed temperature profile of the full station.

The TT support structure consists of two bottom rails and two top rails, which should be aligned within 0.1 mm to prevent damage to the modules by torsion while opening or closing the detector. The alignment included the leveling of the rails as well as the adjustment in x-direction (in the survey coordinate system), where a high precision was obtained using a laser measurement. In the closed position the two halves of the TT station should match each other very well, because the overlapping half modules should not touch the beam pipe isolation. Also the beam pipe has to fit precisely into the hole in the middle of the detector, which demands careful leveling.

To study the thermal behavior of the TT station, an original cooling plate, with a heating load equivalent to that expected from the front end chips, was set in a test environment. The optimal flow rate was determined to be $250\,\ell$/h and the thermal parameters such as the U-value and the pressure drop were estimated. The measured U-values were in the range between (1.1 - 2.4) W/(m^2·K) with large uncertainties for the different test series of the test box and the pressure drop is estimated to be ~ 0.9 bar.

Later the full TT station was installed in the experimental hall in Zürich as a test for the cooling and the assembly of the station at CERN. A detailed study of the thermal parameters at different heating loads was completed. At full heating power the temperature in the station did not exceed $-1.2°$C, which is a good result. The measured U-value was compared to the results of the cooling plate studies and was determined to be 0.55 ± 0.32 W/(m^2·K). After the cooling test the warm up process of the TT station was monitored which took about 6 hours.

1 The TT-station as a part of the LHCb experiment

1.1 CP violation motivating the LHCb experiment

The Standard Model of particle physics characterizes flavor changing processes of quarks with charged-current interactions. Their couplings are described by the complex 3x3 Cabibbo-Kobayashi-Maskawa matrix (CKM matrix). The single phase in the quark mixing matrix generates CP violation. Such CP violating processes lead to a matter-antimatter discrepancy. Since the discrepancy of matter-antimatter in the universe is much bigger than known CP violating processes could explain so far, physicists are interested in exploring the sources of CP violation in more detail and in finding new sources of CP violating processes, such as new particles or new physics. Extensions to the Standard Model of particle physics are required for theoretical consistency and also for explaining astrophysical observations such as dark matter or dark energy. B-mesons are the favored candidates that might unveil new physics and the sources of CP violation. The smallness of the relevant elements in the CKM matrix suppresses the standard tree level decay of B-mesons. This phenomena makes so called penguin and box diagrams accessible to experimental measurements with high statistics. These diagrams, containing internal loops are a very sensitive system for indirect searches for deviations from the Standard Model and thus new physics. If the observable CP asymmetry of processes coming from penguin and box diagrams deviates from Standard Model predictions, this will be a strong indicator for new physics and new sources of CP violating processes. More details can be found in the research plan for LHCb [1].

1.2 The LHCb detector and the Trigger Tracker station

LHCb is a forward spectrometer to study heavy flavor physics and is presently being setup at CERN's Large Hadron Collider LHC. A great strength of the LHCb experiment is the exploration of CP violating processes in a variety of b-flavored particles such as B_d and B_s mesons as well as B-baryons. The expected $b\bar{b}$ production cross section at LHC is $500\ \mu$b. This results in a 3 orders of magnitude larger production rate for b quarks than todays e^+e^- colliders at the nominal LHCb luminosity of $2x10^{32} cm^{-2}\ s^{-1}$. LHCb will also be the first detector collecting statistically significant samples of B_s and other B-flavored hadrons such as Λ_b decays. Studying B-meson decays and other rare phenomena with very high precision, the LHCb detector must have a high track reconstruction efficiency which will be of the order of 95% for charged particle trajectories. A Kaon separation capability for particle momenta from a few to $\sim\ 100$ GeV/c and a very good proper-time resolution of $\sim\ 40$ fs must be provided. Sub-detectors such as the Vertex detector VELO (Vertex Locator) and tracking stations before and after the magnet will permit to reconstruct the trajectories and momenta of the charged particles (Fig 1). The RICH detectors, the electromagnetic and hadronic calorimeters, and the muon stations will be used for particle identification.

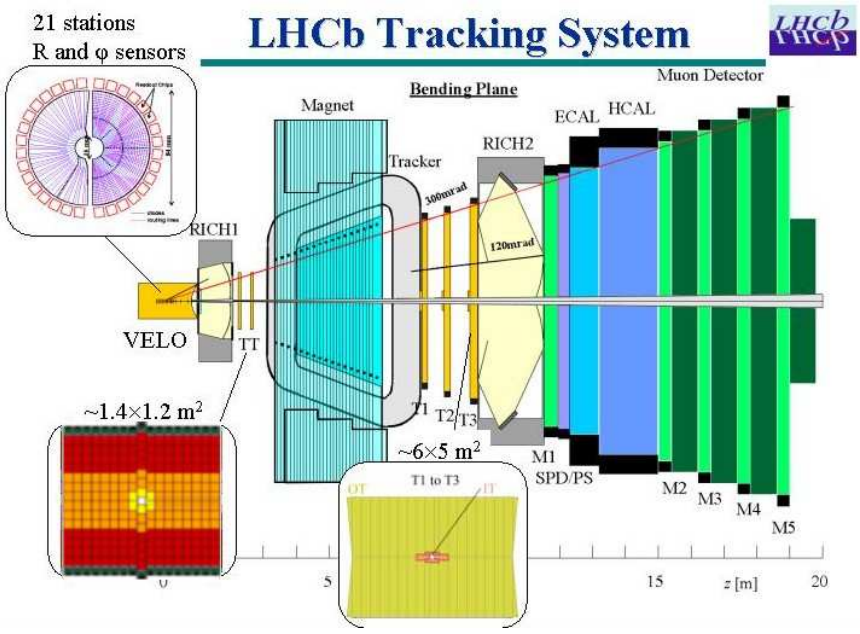

Figure 1: Full LHCb detector with TT-station between RICH1 and magnet [2].

Three tracking stations after the magnet are split in an inner and an outer part. The inner part is based on silicon micro strip detectors. The tracking station in front of the magnet is a large area silicon detector based device. This Trigger Tracker (TT) is a 150 cm wide and 130 cm high planar tracking station located between the RICH1 and the LHCb dipole magnet. It fulfills a two-fold purpose. Firstly, it will be used in the Level-1 trigger to assign transverse-momentum information to large-impact parameter tracks. Secondly, it will be used in the offline analysis to reconstruct the trajectories of long-lived neutral particles that decay outside of the fiducial volume of the Vertex Locator. Also the trajectories of low-momentum particles, bent out of the acceptance of the experiment before reaching tracking stations T1-T3, can be reconstructed. The TT station holds 4 layers in total (at $0°, +5°, -5°, 0°$), with a gap of 23 cm between the second and the third detection layer. This allows a full 3-dimensional track reconstruction. The silicon sensors are produced of single sided p^+-n wafers. Each sensor has a size of 94.4x94.6 mm^2, with 512 strips and a thickness of 500 μm. One detection layer of the TT station is assembled from 17 modules. The modules are lengthwise segmented in half-modules with a 4-3 sensor layout and around the beam pipe with a 4-2-1 readout segmentation. The layout of a half module with 7 sensors and the interconnect cables between sensors and front end hybrid is shown in Figure 2. The sensors are connected to the staggered front end hybrids. All of them are carrying a pitch adapter, 4 beetle readout chips with 128 channels per chip, blocking capacitors and resistors. Mostly 4 sensors are directly connected to the lowest readout hybrid and 3 sensors are connected by the inter-connect cable to the hybrid above. Around the

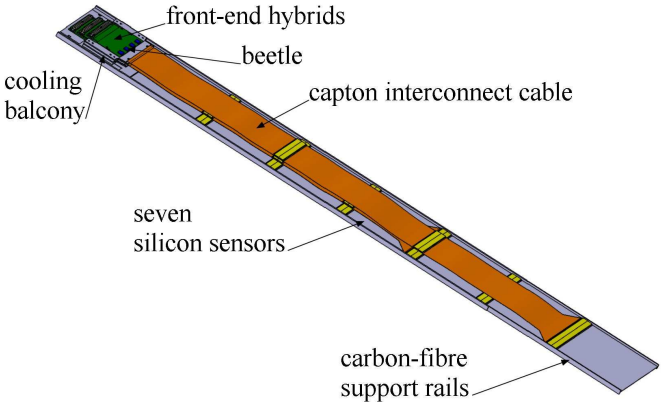

Figure 2: Half-module for the Trigger Tracker detector with a 4-2-1 readout segmentation [3].

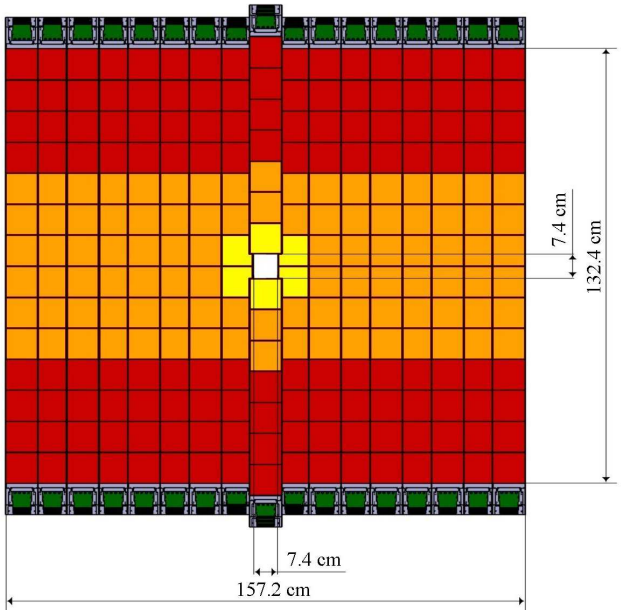

Figure 3: Layer of 17 modules vertically assembled, having on the outer side a 4-3 sensor layout and the 4-2-1 half-modules around the beam pipe [3].

beam pipe 4 sensors are connected to the lowest hybrid, 2 sensors to the second one and 1 sensor to the hybrid on top (4-2-1 readout segmentation, Fig. 2). Two half-modules lengthwise assembled form a module and 17 modules together give a layer (Fig 3). For more details I refer to the Technical Design Report [4] and to the LHCb Note [5]. The LHCb group of the Zürich University accounts for the module production and the full assembling of the TT station.

2 Alignment of the TT Station at CERN

To guarantee a high mechanical precision of the TT station, its support consisting of two rails below and above the station was aligned by the following three devices:

- a leveling instrument for adjusting the height,
- a theodolite for the horizontal alignment,
- a laser system for the high precision measurement of the lower rails.

Before aligning the rails at CERN, the laser system and the leveling method had been tested in Zürich to get an insight on the accuracy. The rails need to be positioned with a high accuracy to facilitate a smooth movement of the station and, more important, to prevent torsion of the modules when closing the station, because the modules are very fragile. Near the beam pipe the inner most 4-2-1 modules of the 5° layers are overlapping with the other half of the station (Fig. 4 and 5). At the

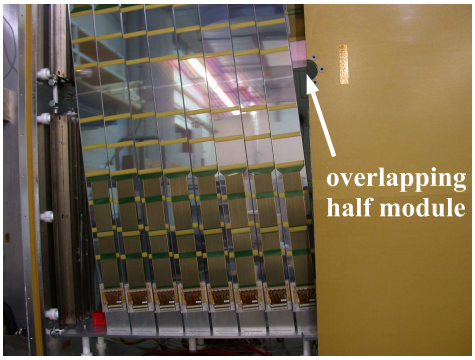

Figure 4: TT station with an assembled 5° layer. The overlapping region can be seen.

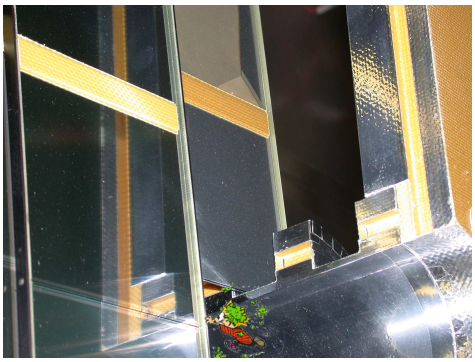

Figure 5: A detailed view from the overlapping 4-2-1 module, sitting in the gap of the beam pipe isolation.

upper and the lower end of the beam pipe isolation small gaps are omitted where these overlapping half modules have to fit in precisely, which is only the case with well adjusted rails. The rail alignment team included the technician Stefan Steiner, postdoc Jeroen van Tilburg and myself.

2.1 Experimental setup

Figure 6 shows a top view of the TT station in in the experimental hall of LHCb at Ferney-Voltaire (F). The rails, each having a length of 3850 mm and a diameter of 40 mm, are placed between the magnet and the RICH1 detector. On the lower and upper rails movable gliders (see Fig. 7) were installed for carrying either the laser's emitter and receiver, the vertically attached ruler for the leveling instrument (leveling ruler) or the ruler for the x-direction. The gliders were leveled with a

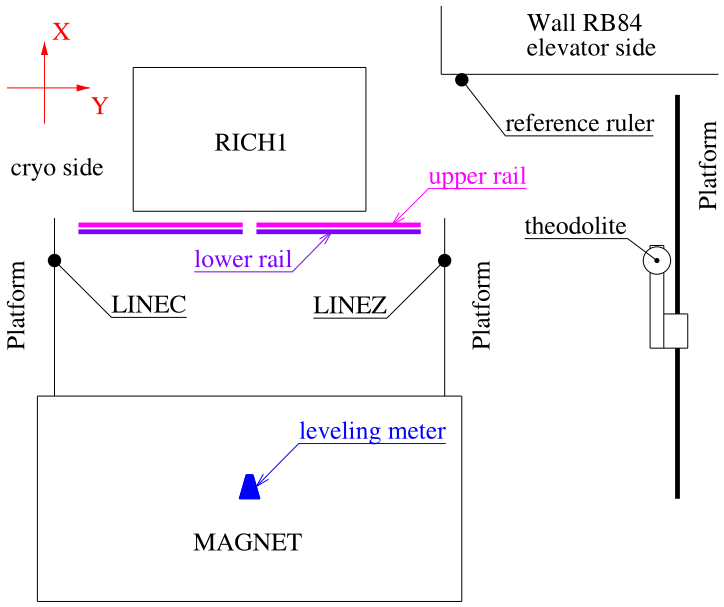

Figure 6: Top view of the area of the TT station in the experimental hall. The theodolite was located on the platform at the elevator side and the reference ruler was attached to the cavern wall opposite the magnet. LINEZ and LINEC are calibration marks for the theodolite. [6]

water-level (resolution 0.1 mm/m). The leveling instrument was located in the magnet, such that it had a view on the full length of the rails and also on the opposite wall of the cavern, where the reference ruler was attached. The position of this ruler was determined in the coordinate system of the survey group (x_{SU}, y_{SU}, z_{SU}) (Fig. 8), which defines the interaction point (IP) at (0,0,0). The CERN survey report sets the zero line of the reference ruler to $z_{\mathrm{SU}} = -0.2026$ m [6]. That means the IP is at a height of $h_{\mathrm{IP}} = 202.6$ mm on the ruler (Fig. 12). The TT station follows the beam axis which has an angle $\alpha = 3.601$ mrad $= 0.206°$ with respect to the x_{SU} axis, which means that the center of the TT-station is higher than the IP (Fig. 8). The displacement c in height is calculated using the distance $d = 2485$ mm from the IP to the center of the TT station along the beam axis in the following way:

$$c = d \cdot \sin\alpha = 2485\,\mathrm{mm} \cdot \sin(0.206°) = 8.95\,\mathrm{mm} \tag{1}$$

The height h_{TT} on the reference ruler for the center of the detector is 211.55 mm.

$$h_{\mathrm{TT}} = h_{\mathrm{IP}} + c = 202.6\,\mathrm{mm} + 8.95\,\mathrm{mm} = 211.55\,\mathrm{mm} \tag{2}$$

For the alignment in x-direction a theodolite was used and a ruler was horizontally attached to a glider (Fig. 9). The position of the theodolite, determined by the CERN survey team, connects the survey coordinate system with the relative

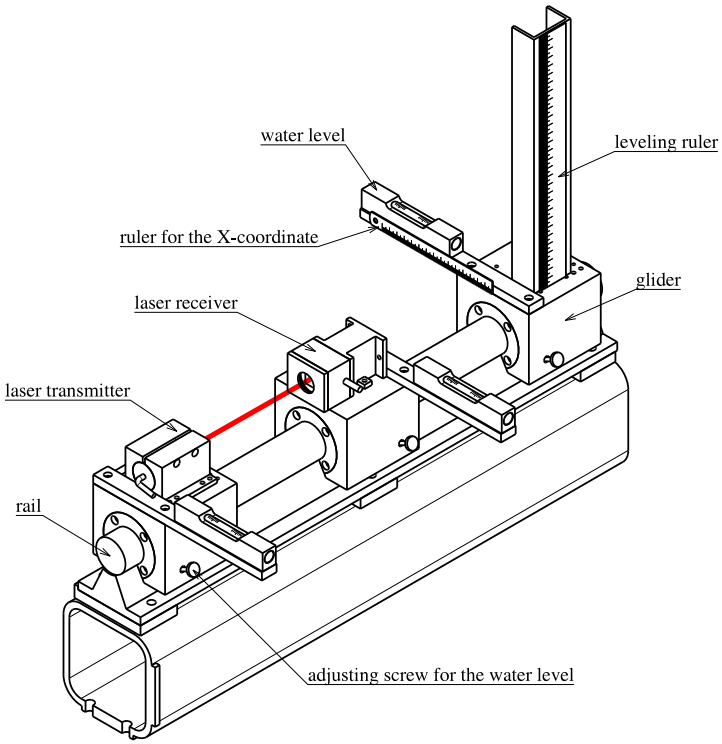

Figure 7: Gliders carrying the water level, the laser transmitter/receiver and the ruler [7].

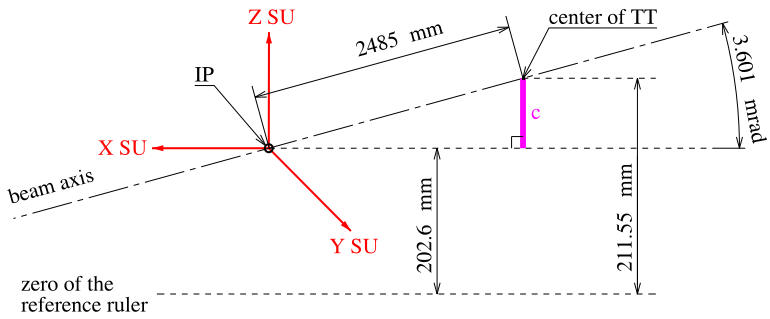

Figure 8: Overview of the survey coordinate system with respect to the beam pipe illustrating the correction made for having the center of the detector at the beam pipe level [7].

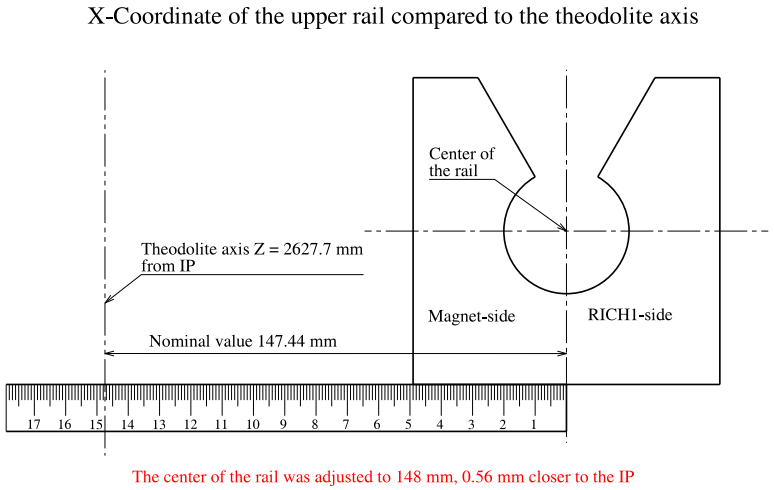

Figure 9: Ruler attached in x-direction to the gliders for reading off by the theodolite [7].

coordinates of the rails. Calibration marks on fixed structures ensured a correct positioning of the theodolite throughout the period of measuring.

The laser system for additional x-alignment was set up of two movable gliders hosting the laser's transmitter and receiver which can be seen in detail in Figure 7. A digital readout device connected the system to the computer, running the readout program. Figures 10 and 11 show two photographs of the scene down in the pit during the laser measurement.

2.2 Data reconstruction and results

2.2.1 Leveling

The leveling instrument was adjusted to a z-position of 211.5 mm on the reference ruler (Fig. 12) for practical reasons (instead of 211.55 mm). The nominal z-position of the detector's center on the leveling ruler was 1330.0 mm, while matching the internal scale i of the leveling instrument to a value of $i_0 = 55 \cdot \frac{1}{10}$ mm. The height measurement was performed usually in steps of 300 mm along the upper and lower rails if the leveling ruler was visible, starting at the cryo side moving toward the elevator side. The relative y-position along the rail is set to $y_{\mathrm{rel}} = 0$ at the far end of the rail on the cryo side. The measured values of the internal scale i were written by hand to a measurement report (see appendix) and processed by the ROOT analysis software. There the following calculation to the raw data was performed to get the deviation d_{Z} from the nominal z-position of the rails (nominal z-position = 0):

$$d_{\mathrm{Z}} = -(i - 55)/10 \tag{3}$$

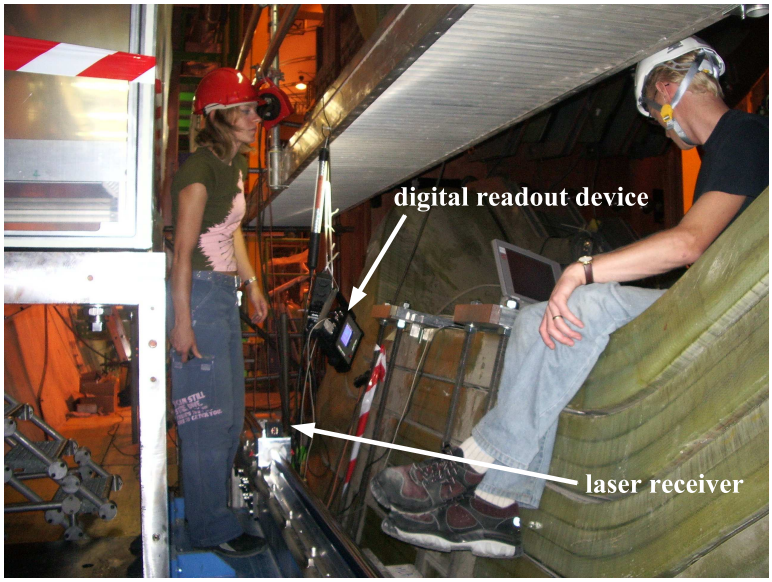

Figure 10: Laser receiver and digital readout device in front of the magnet, while data taking.

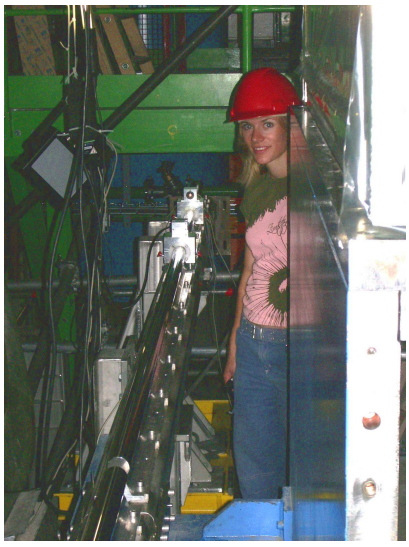

Figure 11: Rail at the cryo side with the laser transmitter and receiver.

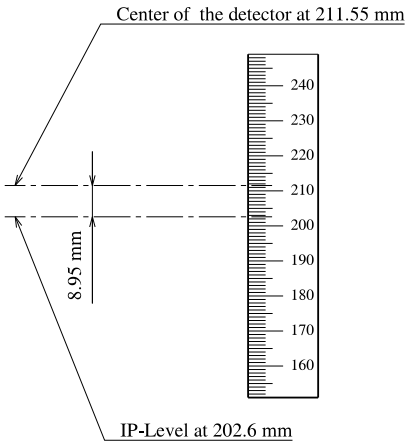

The level of the center of detector was adjusted to 211.5 mm

Figure 12: Reference ruler on the opposite wall of the magnet, giving in particular the center of the TT station according to the coordinate system of the survey group [7].

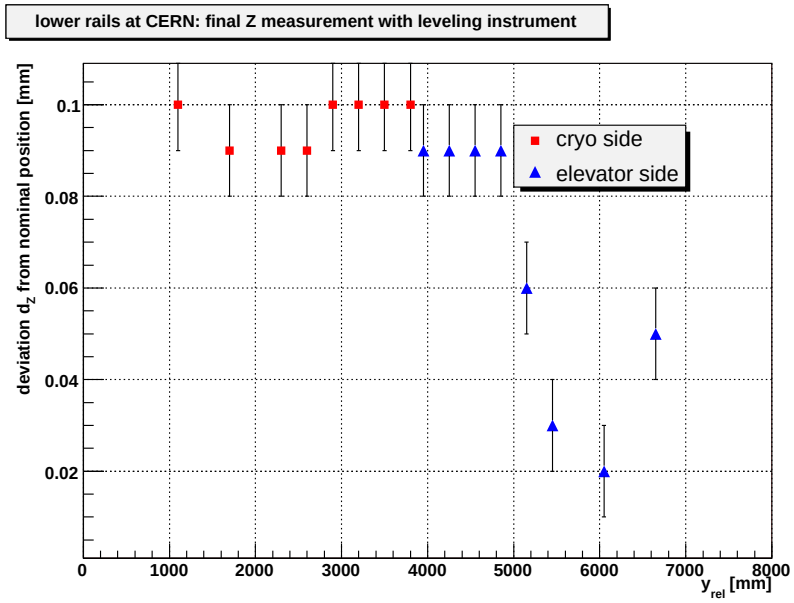

Figure 13: Leveling of lower rail: the zero line is the nominal height of the rails. Both lower rails together are within a variance of 0.1 mm. Comparing to the nominal height they are ~ 0.1 mm too high.

The lower and the upper rails were leveled with a precision of ± 0.01 mm for each data point. Tables 3 and 4 in the appendix show the collected data and Fig 13 and 14 show the final results after adjustment.

Over the full length of both lower rails, which means over a length of ~ 8 m we succeeded to level them with a variance of less than 0.1 mm. Except for the four outermost data points on the elevator side, the lower rails are aligned even within 0.03 mm. It is worth mentioning that the detector itself rests on the lower rails only, thus the well matched lower rails should not pose any problems closing the two halves of the detector. Compared to the nominal z-position the lower rails were put up ~ 0.1 mm too high.

For the upper rails the alignment was much more difficult. The construction of the brackets carrying the upper support structure did not allow a very precise leveling. The possibility of adjusting the upper rail was very limited. For the upper rails an accurate positioning is less important than for the lower rails, because they have a guiding function instead of a supporting and position-defining function. We managed to align them within 1.17 mm, where the rail on the cryo side already contributed most to this difference due to its bent shape (Fig. 14). On the other hand the rail on the elevator side was relatively straight. Compared to the nominal z-position the upper rails were aligned at maximum 0.95 mm too low. With the lower rail a bit too high and the upper rail at maximally 0.95 mm too low the space for the TT station is still within the maximally allowed deviation of 5 mm.

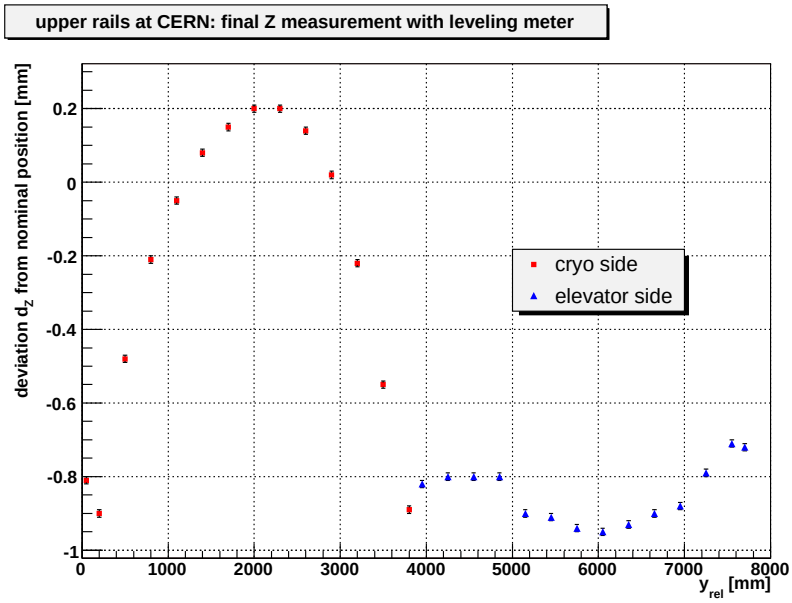

Figure 14: Leveling of upper rail: the zero line is the nominal height of the rails. Both upper rails together are within a variance of 1.17 mm. Compared to the nominal height they are at maximum 0.95 mm too low.

Compared to the nominal z-position the upper rails are located between $+0.21$ mm and -0.95 mm.

2.2.2 Alignment in x-direction

The theodolite axis was at $x_{\mathrm{SU}} = -2.6277$ m [6]. The nominal x-value for the center of the upper rail was 147.44 mm closer to RICH1 than the theodolite axis (see Fig. 9) and similarly for the lower rail 137.99 mm closer to the RICH1. Since these nominal positions were quite difficult to read with the theodolite with accurate precision, it was decided to adjust the value of the upper rail to 148 mm and of the lower rail to 138.5 mm. This means the whole TT station was shifted ~ 0.5 mm closer to the RICH1 detector than designed. The measurements were performed usually in steps of 300 mm (± 15 mm) along the upper and lower rails, as long as the horizontal ruler was visible. The x-alignment of the rails was simultaneously monitored through the theodolite and adjusted to the nominal x-value. As in the previous leveling measurement the measured values of the horizontal ruler were written by hand to a measurement report (appendix) and processed by the ROOT analysis software. There the following calculation to the raw data was performed to get the deviations d_{Xup} and d_{Xdown} from the nominal x-position of the rails (nominal x-position = 0):

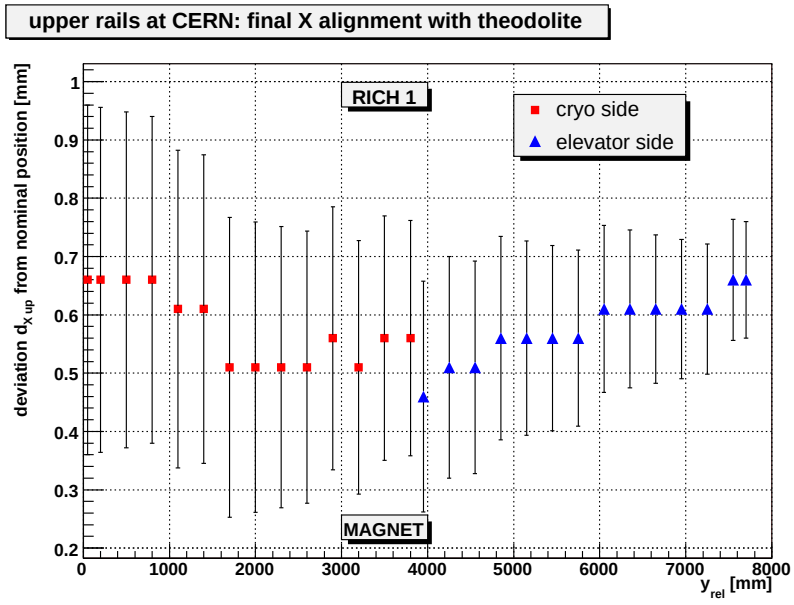

Figure 15: x-alignment of upper rail with the theodolite

upper rail:

$$d_{\mathrm{Xup}} = data - 147.44 \tag{4}$$

lower rail:

$$d_{\mathrm{Xdown}} = data - 137.99 \tag{5}$$

Tables 5 and 6 in the appendix show the collected data and Fig. 15 and 16 show the results.

With the theodolite the personal bias in reading the ruler was quite large compared to the leveling instrument. The larger the distance between the glider and the theodolite the more difficult the read off. A precision between ± 0.1 and ± 0.3 mm was achieved for the reading, linearly decreasing from the far end of the cryo rail to the far end of the elevator rail. The read off error e_{x} is calculated by linear interpolation in the following way:

$$e_{\mathrm{x}} = a \cdot y_{\mathrm{rel}} + b \qquad \text{with} \quad a = -2.614 \cdot 10^{-5} \quad \text{and} \quad b = 0.301\,\mathrm{mm} \tag{6}$$

The systematic error due to personal bias is estimated to be ± 0.5 mm. The special alignment on 148.0 mm respectively 138.5 mm adds a global offset from the nominal x-position. As the lower rail was readjusted using a laser system with much higher precision, the larger variance of this measurement was less important. As for the height measurement, the upper rail has more of a guiding function and was therefore not aligned with the laser.

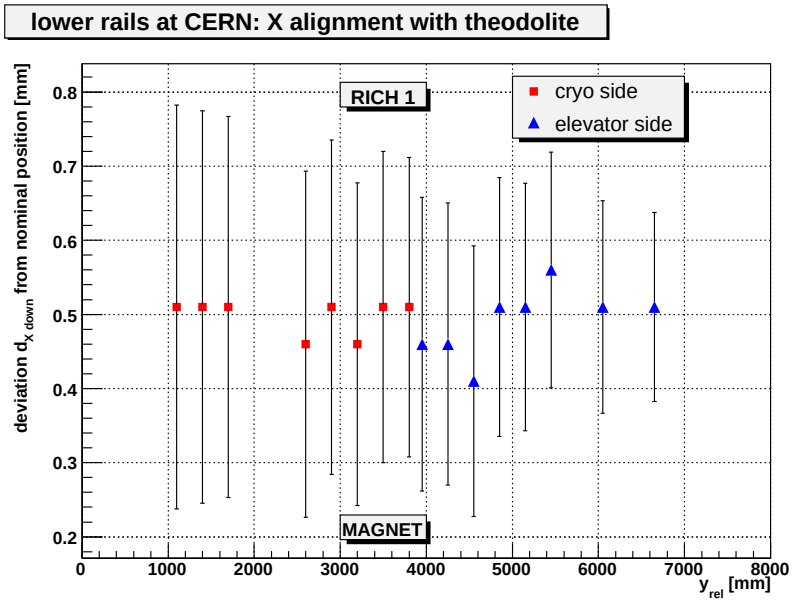

Figure 16: x-alignment of lower rail with the theodolite

2.2.3 Alignment with the laser system

The laser alignment system was read out by a computer running a data taking software. The program takes 120 data points over ~ 30 s measuring time, calculates the mean value and stores it in a table. The laser system was calibrated such that at the minimal and maximal distance the read out value was set to zero. This defined the axis of the laser beam. The relative x-alignment of the rails was simultaneously monitored by the readout device and adjusted when needed. The data was processed by the ROOT analysis software.

Table 7 in the appendix shows the collected data of the laser alignment in x-direction of the lower rails. Figure 17 shows the same results. Although the laser system allowed for a fast and accurate alignment along the rail axis, however, the mechanical manipulations of the large scale structure of the rail was difficult for this range of precision. The readout device of the laser system responds to the slightest movement of the rail such as touching it or walking around near the rail. In case other people were working with machines in the vicinity of our area, the measured values were influenced and no reliable measurement was possible. Also the adjustment at one position along the rail influenced the whole rail, due to the rigidity of the rails itself. Taken all these effects into account, the final precision was estimated to be ± 0.02 mm. For both lower rails we succeeded to align them with a maximal variance of 0.135 mm with a tendency towards the magnet. This guarantees a very smooth movement for the TT station as was successfully tested 4 months later when it was put on the rails.

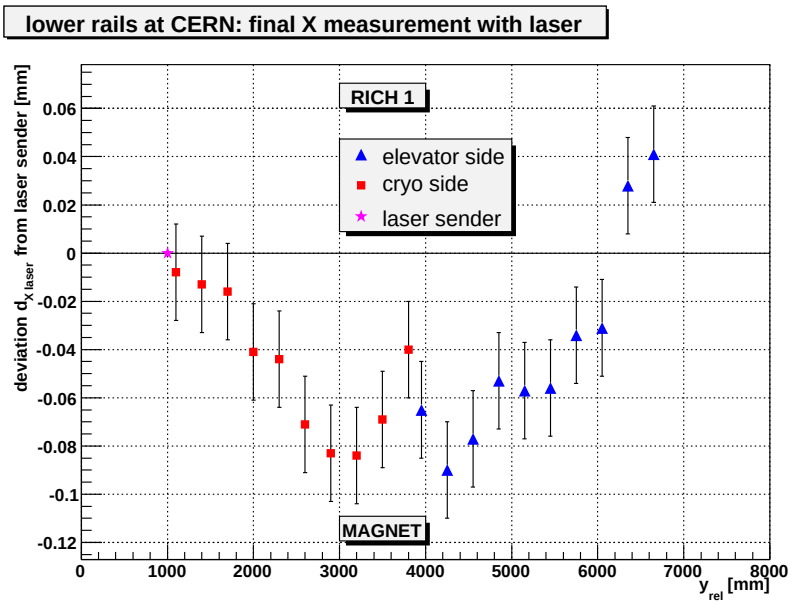

Figure 17: Relative laser alignment of lower rail in x direction. The zero line is the reference system of the laser. Both lower rails together are within an accuracy of ± 0.1 mm with a tendency towards the magnet.

3 Thermal studies in the test box

The purpose of the cooling system of the TT detector is to remove the dissipated heat from the front end hybrids and to maintain the detector modules at a constant temperature of about $5°C$ during operation. An original detector cooling plate, populated with temperature sensors and equipped with heaters to simulate the heating load of the beetles was used for thermal studies. These studies provided a detailed temperature profile which led to a construction improvement of the cooling plate. The following thermal data was collected with a support of Stefan Steiner:

- Pressure drop in the cooling plate
- Temperature profile at different heating loads
- heat transfer coefficient of the test box
- Temperature profile at different flow rates

3.1 Experimental setup in the assembly hall 36G38

Figure 18: Chiller (left) connected to the test box with insulated tubes.

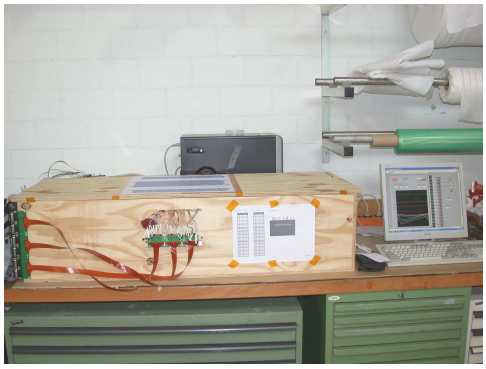

Figure 19: Test box with cooling plate inside. The cables of the temperature sensors were routed to the outside and plugged into a patch panel print.

The setup in the assembly hall 36G38 at the University of Zürich consisted mainly of a wooden box (test box, see Fig. 19) with a 40 mm thick AIREX® R82 insulation inside. In the test box an original cooling plate, made of aluminum with dimensions of $\sim$ 900 mm x 350 mm (Fig. 20), was placed. Both cooling lines of the plate were connected to isolated plastic hoses which led to a recirculation chiller (Fig. 18). The customized chiller was from LAUDA, model WKL 10000 W, with a designed pumping capacity of $3600\,\ell$/h, an overpressure safety valve and suitable for the cooling fluid C_6F_{14}. On the cooling plate so-called balconies were assembled, serving now as a heat conductor and later also as a support for

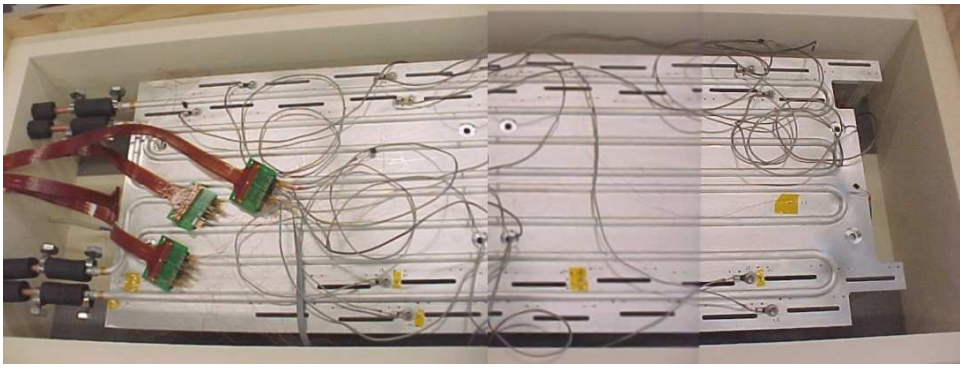

Figure 20: Inside of the test box with the cooling plate, having two cooling lines and being populated with PT1000 temperature sensors.

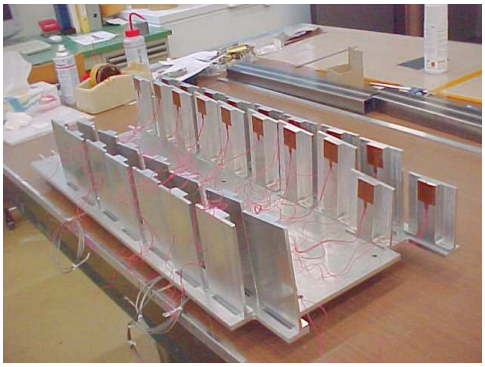

Figure 21: Cooling plate upside down with the assembled balconies serving as the module support structure. Kapton heaters were attached to every balcony to simulate the heating load of the beetles.

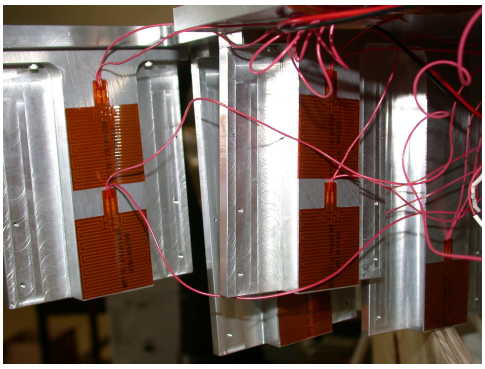

Figure 22: Detailed view of balconies closest to the beam pipe. They have an additional heater simulating the bigger heating load of the 4-2-1 modules.

the silicon modules. On their front-end hybrids the modules carry up to 12 beetles, producing the heating load of up to 0.8 W per chip. Kapton heaters were glued to the balconies (Fig. 21 and 22) simulating the heating load of the beetles. The cooling plate inside the test box was populated with 46 PT1000 temperature sensors and a combined temperature/humidity sensor was freely suspended in the box. For the detailed positioning of the PT1000 sensors see chapter 3.5. Four different types of PT1000 sensors were used in the setup, all of them with two connection leads:

- Type A: screw-able Nickel plated copper sensor, with 6.7 mm ring lug from manufacturer MINCO, model S101732 (Fig. 24).
- Type B: 1.3 x 1.7 mm ceramic sensor from manufacturer MINCO, model S102404 (Fig. 24).

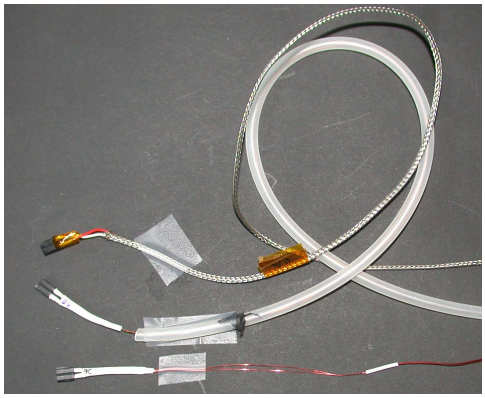

Figure 23: Plug of the PT1000 sensors Type A, B and D.

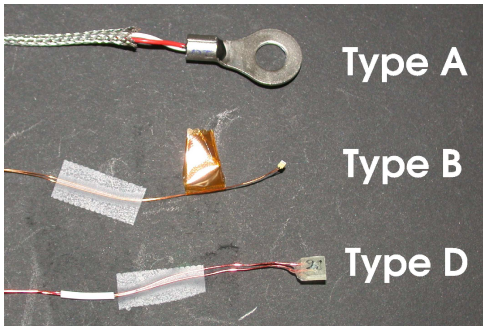

Figure 24: Types A, B and D of the PT1000 temperature sensors.

- Type C: SMD style PT1000 sensor, 1.3 x 2.0 x 0.5 mm from manufacturer JUMO GmbH & Co. KG Germany, type PCS 1.1302.10 [10]
- Type D and E: PT1000 of type C encapsulated with Araldite (Fig. 24).

All sensors were of DIN tolerance class B with a permissible deviation of $\pm(0.3 + 0.005 \cdot |T|)$, where T is the temperature in °C [11]. Sensors of type A were screwed to the cooling plate and all the other sensors were attached with adhesive Kapton tape unless otherwise noted. All wires of the sensors were routed to the outside of the test box through a small slot and plugged into a patch panel (pp).

The combined temperature/humidity sensor was of type HMX2000-HT™from Hygrometrix Inc. The manufacturer provided calibration data for the sensors and suggested in Application Note [12] a calibration procedure with interpolation using a 2^{th} order polynomial. However, the working temperatures of the sensors during the measurement were outside the quoted range of the calibration data, therefore the humidity values that are given in this thesis are un-calibrated and their accuracy is not known.

To prevent condensation inside the test box during cooling and warm up, dry air was purged through the box. In the beginning only a minimal air flow was chosen for not warming up the box too much by dry air purging. Later the air flow was optimized.

3.2 Data reconstruction

The PT1000 sensors were all connected to the pp inside prints. From there a Kapton cable connected to the second pp outside print of the test box with two serial port connectors. Serial cables 1:1 matches the data acquisition board and the National Instruments PCI-6225 data acquisition card in the computer (Fig. 25).

The temperatures were measured by means of a Wheatstone bridge (Fig. 26). By changing one of the resistances (the temperature sensor), a potential difference

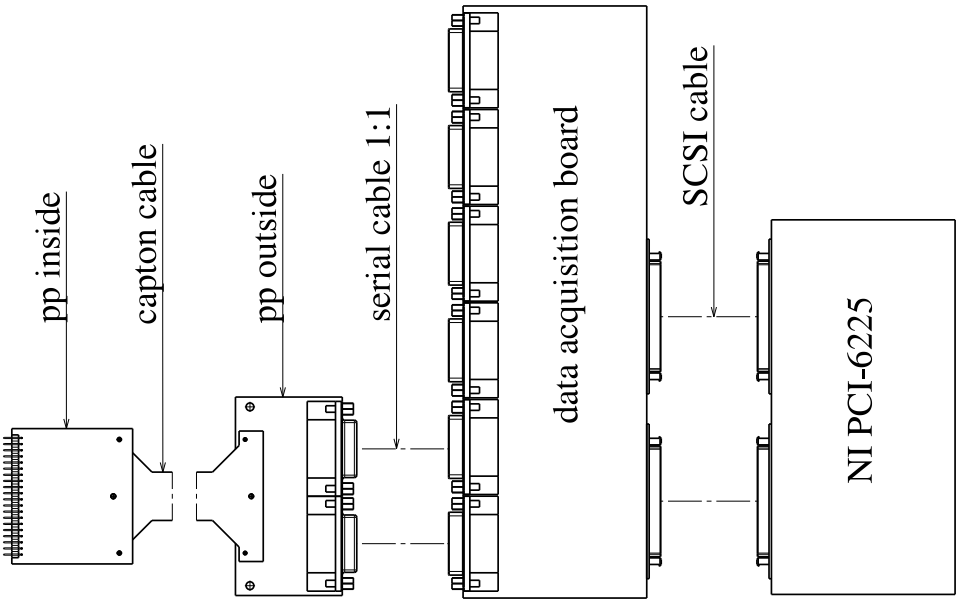

Figure 25: Data acquisition: the PT1000 sensors were connected to the patch panel (pp) inside print. A Kapton cable led to the pp outside print and from there serial 1:1 cables transfer the signals to the data acquisition board. A NI PCI-6225 card represented the final element in the chain and was connected via SCSI cables [7].

is generated at the bridge (U_{AB}). The unknown resistance R_1 can be calculated:

$$R_1 = \frac{R_4}{(\frac{R_2}{R_3+R_2} - \frac{U_{\mathrm{AB}}}{U_{\mathrm{in}}})^{-1} - 1} \tag{7}$$

U_{in} is the input voltage which is obtained directly from the computer and amounts to ~ 5 V. The temperature is calculated with the following formula using the measured resistance R_1:

$$T = \frac{R_1 - R_0}{K} \tag{8}$$

where R_0 is the resistance of a PT1000 at 0°C and K is the temperature coefficient. The precision of all resistances is well known.

The program LabVIEW was used with a virtual instrument (VI) called TT-TempRH.vi from Ueli Bieler. Any further information for the readout via this VI can be found in his work report [8]. The VI was modified such that the collected data was written to a comma separated list (.csv format) with the exact date (year, month, day, hour, minute, second) for every data point. Later the readout of two flow-meters was achieved. For further analysis the ROOT software was used.

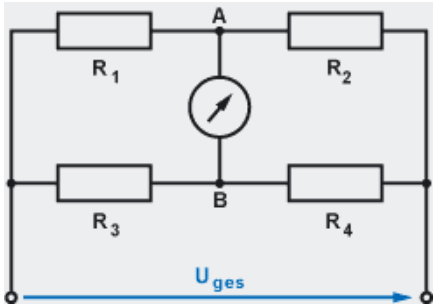

Figure 26: Wheatstone bridge [9].

Figure 27: Calibration of PT1000 sensors in ice water.

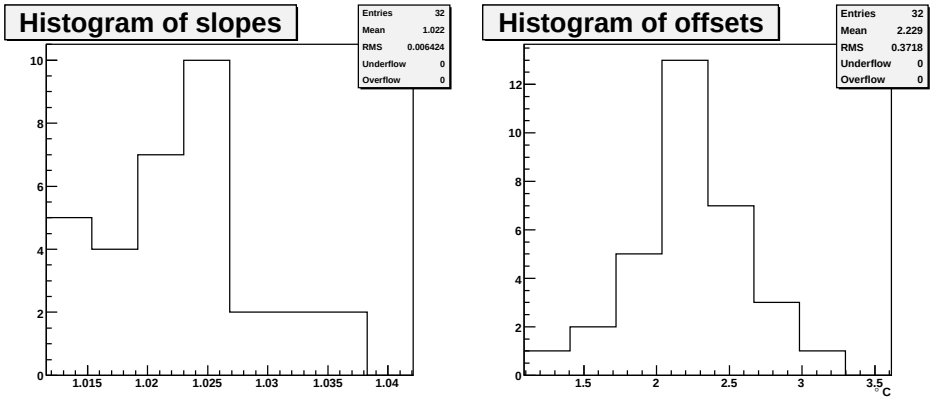

Figure 28: Calibration results: The offsets with mean 2.229 were corrected in the software while the slopes were left uncorrected.

3.3 Calibration

A previous test[1] pointed out that a calibration of the temperature sensors is essential. Thus the sensors were calibrated in ice water ($0°$C) and in water of $22.5°$C (see Fig. 27). A line was fitted through the $0°$ C and 22.5°C to determine the slope and the offset of all waterproof sensors (32 out of 46). The non waterproof sensors[2] were corrected with the mean of the offset data, because a similar offset was observed during the previous experiment. Non waterproof sensors were especially of type B and C. For B1 and B4 a calibration was made because they were broken and replaced with D type sensors while the original name was kept. The effect of the average slope of $s = 1.022$ on the measured temperatures is smaller than the measuring uncertainty of the temperatures, therefore the slope was not corrected ($s = 1$). With a mean of $2.229°$C (Fig. 28) the offset is large compared to the measuring error.

Having about twice as much sensors than pins to plug them in, the sensors were split up in 2 configurations (A and B) and plugged every time at exactly the same position at the pp inside print. The reason was that a correlation between the plug position and the offset could not be excluded at that time. The detailed results can be seen in Table 8 in the appendix.

3.4 Pressure drop of the cooling plate

In an early experimental setup the functionality of all components was tested with the chiller for the burn in tests, since the setup with the other chiller (mentioned

[1] This experiment is presented in more detail together with the pressure drop measurement in chapter 3.4.

[2] An attempt was made to calibrate sensors of type B but some of them died during the calibration, either through coldness shock or drowning.

Figure 29: Pressure gauges at the cooling system of the early setup.

in chapter 3.1) was not implemented at that time. This chiller provided pressure gauges as shown in Fig. 29. The pressure drop Δp in one circuit of the cooling plate is needed to estimate the pressure drop of the full TT station. The CERN cooling team will use this estimate to adjust the pressure of the cooling system in our area. The whole station is designed to have all cooling circuits in parallel, so the measured pressure drop of one circuit gives a rough estimate for the pressure drop of the full station, excluding the supply lines to the cooling plates. A theoretical estimate of Δp was calculated beforehand [13] using the Colebrook formula:

$$\Delta p = f(Re, k, d) \cdot \frac{l}{d} \cdot \rho \cdot \frac{\upsilon^2}{2} \tag{9}$$

where d is the hydraulic diameter, l the pipe length, ρ the density of the cooling fluid, υ the mean velocity of the cooling fluid and $f(Re, k, d)$ is the friction coefficient depending on the Reynolds' number Re, the roughness of the pipe k and the hydraulic diameter. The bending of the pipe and the static pressure is disregarded in the Colebrook formula. The theoretical pressure drop was estimated to be 0.4 bar at $240\,\ell$/h at one circuit of the cooling plate.

In a series of measurement the pressure drop along one circuit of the cooling plate was estimated using the following devices installed in the setup:

- **IR-Opflow** turbine flow meter of manufacturer Beli Technics, Wijchen (NL) with an optoelectronic infrared detector and an allowed flow range of 18-540 ℓ/h. The accuracy is $\pm 3\%$ of the measured value.
- **rotameter** with a floating body giving the flow on a mm scale. The read off precision is ± 2 ℓ/h.
- **pressure gauges** from manufacturer Bourdon-Haenni, EN-837-1 Class 1, with a read off accuracy of ± 0.02 bar.

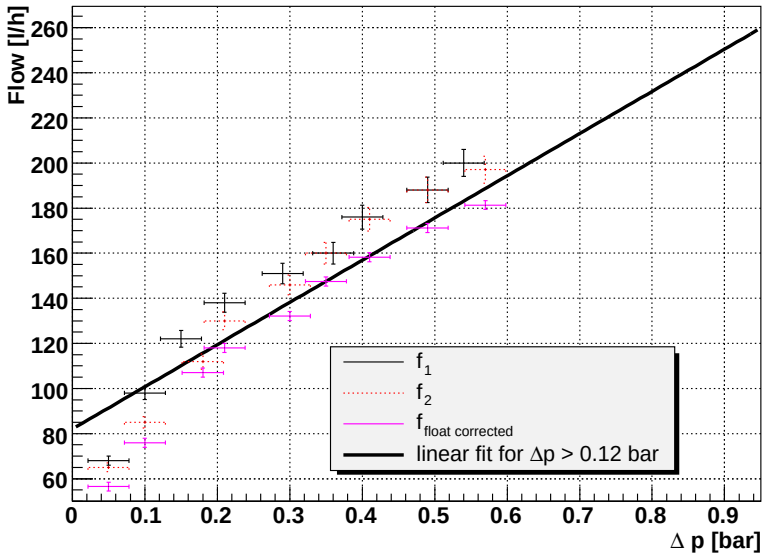

Figure 30: Results of the pressure drop measurement. At the extrapolated nominal flow of $250\,\ell$/h for the full station, the pressure drop amounts to ~ 0.9 bar.

Two test series were accomplished:

1. the incoming pressure $p_{1\mathrm{in}}$, the outgoing pressure $p_{1\mathrm{out}}$ and the turbine flow rate f_1 were measured simultaneously.

2. the incoming pressure $p_{2\mathrm{in}}$, the outgoing pressure $p_{2\mathrm{out}}$, the turbine flow rate f_2 and the rotameter flow rate f_{float} were measured simultaneously.

The IR-Opflow turbine flow meters were tested whether they make any difference in measuring C_6F_{14} or water, but no difference was found and a re-calibration on C_6F_{14} was not required. The rotameter flow rate f_{float}, however, is calibrated on water. The values were corrected for the cooling fluid C_6F_{14} with a calibration coefficient measured by Michael Dimmler [14] using the same cooling system:

$$f_{\mathrm{float\,corrected}} = 0.0007 \cdot f_{\mathrm{float}}^2 + 0.7462 \cdot f_{\mathrm{float}} + 9.2073 \quad . \tag{10}$$

The pressure drop Δp was calculated as following:

$$\Delta p = p_{\mathrm{in}} - p_{\mathrm{out}} \quad , \tag{11}$$

where the error on Δp is determined by common error propagation and amounts to ± 0.028 bar. Since the chiller had a maximal pumping capacity of $200\,\ell$/h the data was linearly extrapolated to the nominal flow for the full station which is $250\,\ell$/h. For the extrapolation only data points with $\Delta p > 0.12$ were used which are clearly

in the turbulent region. The pressure drop of one circuit of a cooling plate for a flow rate of $250\,\ell$/h is estimated to be $\sim\ 0.9$ bar as shown in Figure 30. Note, that the measurement includes a pressure drop of 0.4 bar coming from the installed IR-Opflow turbine device [15]. Subtracting these 0.4 bar from the measured value of 0.9 bar the pressure without the flow meter amounts to 0.5 bar which is close to the estimated 0.4 bar from the Colebrook formula.

The data points indicate a slight discrepancy between the turbine flow and the rotameter for a fixed Δp. The reason of this difference was not further investigated since an uncertainty on the true flow rate of 20% was found to be sufficient for the purpose of the study.

3.5 Temperature profile

The goal of distributing 46 temperature sensors on the cooling plate was to generate a temperature profile for monitoring the ongoing thermal procedures of a cooling plate under different circumstances. As there was no information on where the biggest temperature changes will occur, the sensors were placed at all possibly interesting spots. For a detailed view of the distribution see Figure 31. The first

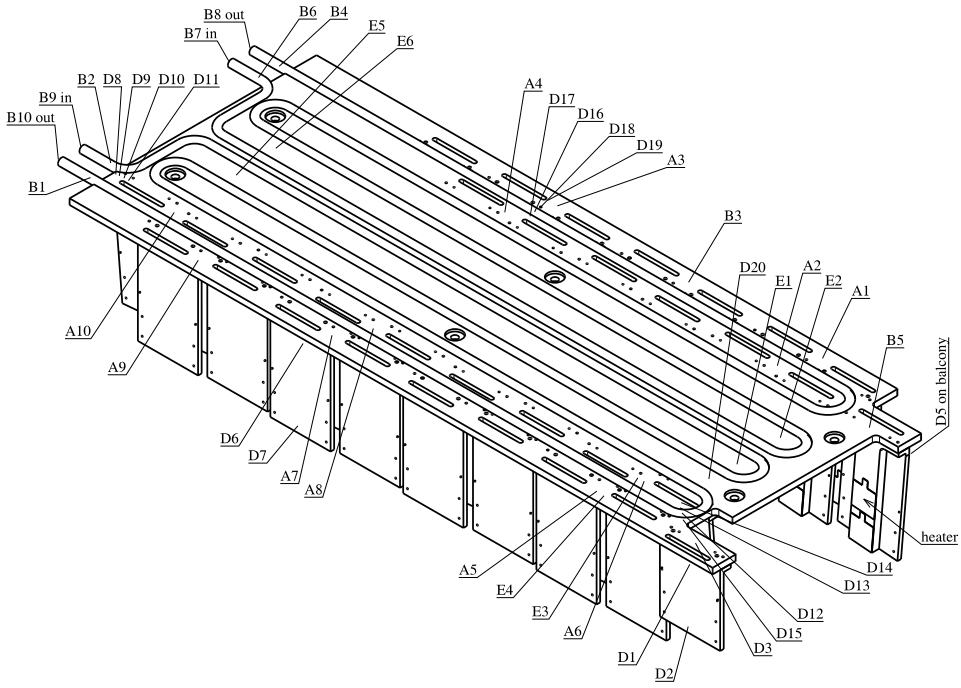

Figure 31: Plan of the exact allocation of the PT1000 sensors [7].

requirement was to have some sensors uniformly distributed over the whole plate. Next the inlet and outlet temperatures were measured directly by B7-B10 which were placed in the fluid. At the nearest position to the cooling supply, sensors were placed on the tube (B1, B2, B4, B6) to get a feeling for the thermal resistance of

the pipe by comparing the temperatures in the fluid with the ones on the pipe. The next group of sensors was placed to register the temperature drop perpendicular to the cooling pipe. Three such groups had been assembled: D8-D11, D12-D15, D16-D19. Some sensors had a control function and were placed close to another sensor (i.e. E4 controlled A5). That information revealed the need of calibration. Quite of interest was the heat transfer from the top of the balconies to the cooling plate. Therefore, sensors were placed on the balconies on the other side as the heaters (i.e. D6 and D7). In the region near the beam pipe many sensors were placed. Since the maximum heating load was expected there additional heaters on the balconies were added to simulate the higher heating load of the beetles at the 4-2-1 modules.

3.5.1 Heating load measurements

These test series were performed with the following basic settings: the nominal temperature of the cooling fluid C_6F_{14} was set to $-15°C$ with an average flow rate of $250\,\ell$/h. Room temperature was between $23°C$ and $25°C$ and the cover of the test box was always closed during data taking. A test series comprised of first a measurement without any heating load ($P = 0$ W), then the power P was increased in steps of 50 W to 200 W. The last step was to 230 W and after that, the additional heaters near the beam pipe were switched on with a power of 10 W (making the total power $P = 240$ W). After increasing the power, the system was brought to thermal equilibrium, which took about half an hour. Each data taking period was limited to ~ 6 min, collecting roughly 1000 data points. Five different test series were accomplished with the above mentioned basic settings:

1. **cooling measurement:** no dry air was blown through the test box.

2. **cooling with air:** dry air was blown through the box but with the smallest noticeable flow.

3. **cooling with copper:** in the TT station a large number of Kapton cables with copper traces are dangling out of the box. To estimate the potential heat attack, the cable mock up was prepared consisting of copper strips with the same cross section as foreseen in the final design (Fig. 32) which amounts to ~ 1 mm^2. The dry air flow was increased by a small amount.

4. **cooling with copper and heat conduction:** the copper dangling out of the test box was exactly the same as in the previous measurement. The cover was pressed down with an lead brick for a better fit. At the previous test series it was found out, that at the edge of the cooling plate near the beam-pipe the heat was not transported well to the cooling pipe. So this exposed region got much warmer than the rest of the plate. To prevent this, the effective cross section of the cooling plate was enlarged by a thick copper cable of ~ 1 cm diameter (heat conduction). The dry air flow was significantly increased.

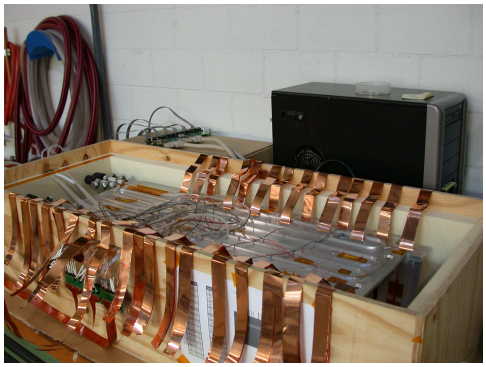

Figure 32: Experimental setup for the test series cooling with copper. Copper strips were dangling out of the test box, simulating the Kapton cables for one cooling plate at the station.

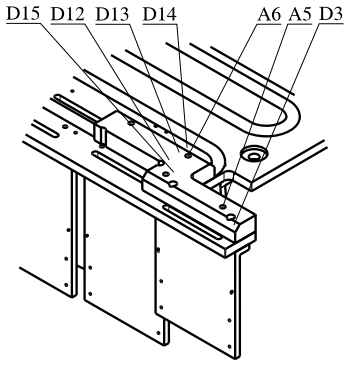

Figure 33: New cooling booster designed to improve the heat transfer from the foremost balcony to the cooling pipe [7].

This test series was shortened to measurements at $P = 0, 100, 200, 230, 240$ W.

5. **new cooling booster:** the thick copper cable enhanced the heat flow so much that a permanent solution was designed for enlarging the cross section at the exposed region. With this so called new cooling booster (Fig. 33), the test series was repeated but without the copper strips and was shortened to $P = 0, 240$ W.

Based on the data a temperature profile of the cooling plate was created for each power setting to identify potential broken or not working sensors and to spot the interesting temperature regions. In total 24 out of 46 sensors are plotted: sensors D8-D11 in the region of the cooling supply line, the sensors D16-D19 in the central region of the cooling plate, the sensors at the exposed region near the beam pipe, and the sensors at the balconies. The results for the cooling with air are shown in Figure 34. The four other test series are plotted in the appendix (Fig. 41, 42, 43 and 44). Table 1 gives an overview of the discussed data for the different test series. The table shows beside the box temperature and the humidity three temperatures: the coldest close to the entrance of the cooling supply (D8), the warmest close to the center of the TT station (D3) and a typical temperature (A7).

The results of the first two test series are very comparable: the temperatures on the cooling plate show almost no difference between no dry air flow and a small dry air flow. But the test box temperature itself increased from $-7.8°$C to $-7.2°$C at $P = 0$ W and from $-1.2°$C to $-0.5°$C at $P = 240$ W. The dry air had a positive influence since it reduced the relative humidity in the test box by 10%. At the group of sensors near the beam pipe, the $\Delta T = |T_{\text{sensor}} - T_{\text{inlet}}|$ was the highest, excluding the balconies. Because this exposed region around D3 has a relatively

Table 1: Overview of the data from the test box measurements at $P = 240$ W

test series #	T_{box} [°C]	Humidity [%]	T_{D8} [°C]	T_{D3} [°C]	T_{A7} [°C]
1	-1.2	59	-12.1	+4.2	-9.9
2	-0.5	49	-12.1	+4.5	-9.5
3	+1.1	41	-11.9	+5.3	-9.3
4	-1.3	27	-11.4	-1.5	-8.9
5	-4.3	30	-12.6	-5.0	-9.6

small cross section of material leading the heat to the cooling pipe, temperatures increased much more than at other regions on the plate. For instance the opposite sensor B5, also at quite exposed position, shows the same temperature as D15 sitting right next to the cooling pipe.

The third test series with the copper strips showed a slight raise in the temperatures of at most $1°$C and a decrease of the humidity of 8%. The small increase of the dry air seemed to influence only the humidity. The increase of the temperatures was accredited to the copper strips transferring heat (60 W [13]) from the outside and also to the fact, that the cover was not sitting as tight on the test box as without copper strips. The box temperature at $P = 240$ W rose to $+1.1°$C.

The fourth measurement with the increased cross section by a thick copper cable showed more pronounced effects: the temperature of the most exposed sensor D3 decreased to $\sim 7°$C at full power, and the heat transfer from the balcony near the beam pipe to the cooling plate was much better. With the better fitting cover the box temperature decreased to $-1.3°$C at full heat load and the humidity was decreased drastically from 41% to 27% by the larger air flow.

With the new cooling booster the temperature of sensor D3 was decreased again by $\sim 3°$C and the heat transfer from the most exposed balcony to the cooling plate also increased. The obtained box temperature amounted to $-4.3°$C at full heating load, which is a very promising result and gave reason to expect a temperature below zero also for the full station tests. With a humidity of 30% no condensation occurred in the box over the entire measurement.

3.5.2 U-value of the test box

The heat transfer rate of the cooling system $\dot{Q}_{\mathrm{cooling}}$ depends on the heat capacity $C_{\mathrm{C_6F_{14}}}$ of the cooling fluid $\mathrm{C_6F_{14}}$ type PF5060 of manufacturer 3M [16], the mass flow $\dot{M} = \rho_{\mathrm{C_6F_{14}}} \cdot \frac{dV}{dt}$, and the temperature difference of ingoing and outgoing cooling fluid $\Delta T = |T_{\mathrm{in}} - T_{\mathrm{out}}|$.

$$\dot{Q}_{\mathrm{cooling}} = C_{\mathrm{C_6F_{14}}} \cdot \dot{M} \cdot \Delta T = C_{\mathrm{C_6F_{14}}} \cdot \rho_{\mathrm{C_6F_{14}}} \cdot \frac{d\mathrm{V}}{dt} \cdot |T_{\mathrm{in}} - T_{\mathrm{out}}| \qquad (12)$$

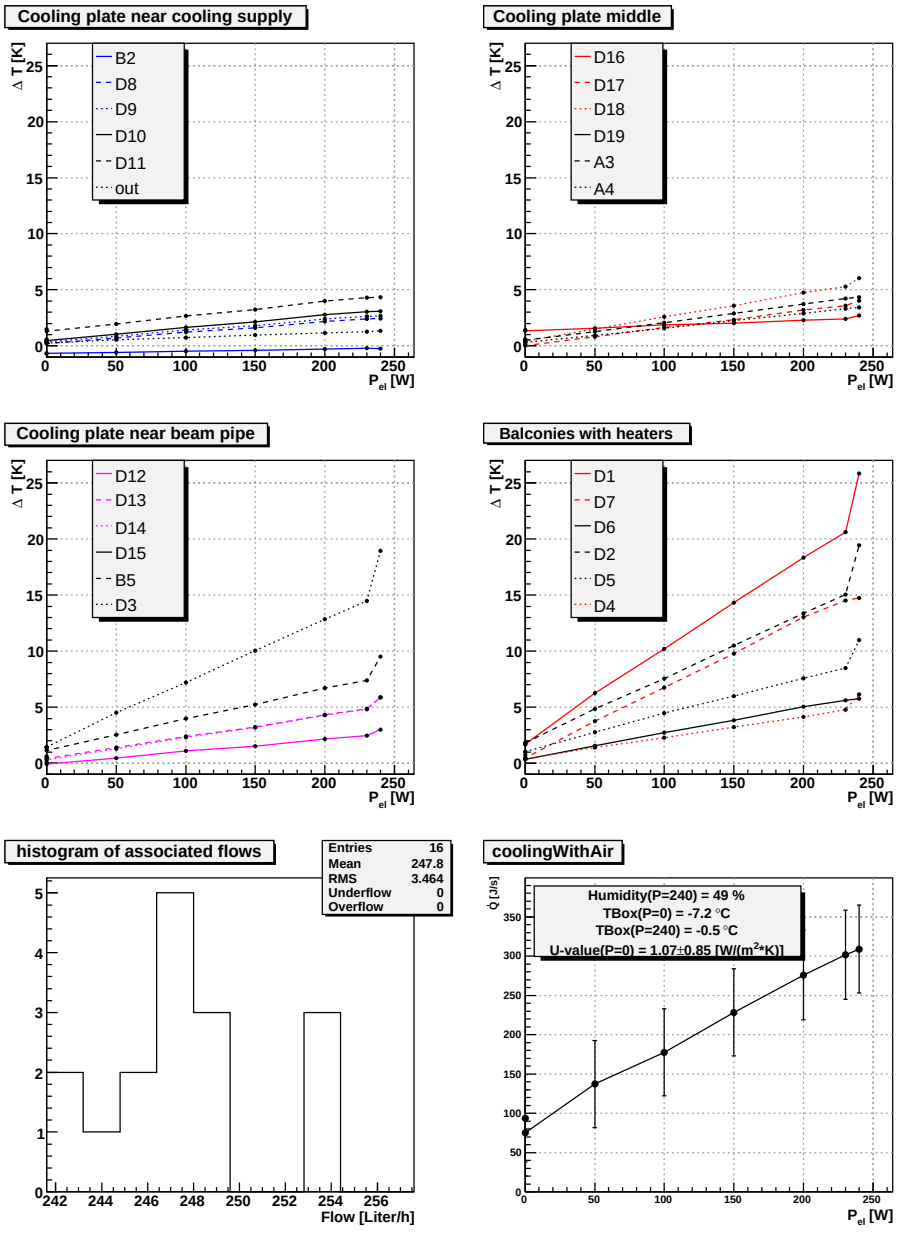

Figure 34: Results of the cooling with air measurements. Sitting on a balcony with two heaters, D1 was the warmest sensor with a ΔT of $\sim 25°$C which corresponds to an absolute temperature of $\sim 10°$C.

Table 2: Summary of the U-values

test series #	U [W/(m^2 · K)]
1	1.05 ± 0.85
2	1.07 ± 0.85
3	1.41 ± 0.96
4	1.76 ± 0.98
5	2.42 ± 1.10

with $\rho_{C_6F_{14}}$ the density of C_6F_{14} and $\frac{dV}{dt}$ the flow rate. ρ and C were calculated according to [16].

$$\rho_{C_6F_{14}} = (1740 - 2.61 \cdot T) \quad \frac{\mathrm{kg}}{\mathrm{m}^3} \tag{13}$$

$$C_{C_6F_{14}} = (1014 + 1.554 \cdot T) \quad \frac{\mathrm{J}}{\mathrm{kg} \cdot^{\circ} \mathrm{C}} \tag{14}$$

with $T = \frac{T_{\mathrm{in}}+T_{\mathrm{out}}}{2}$ given in °C. The total heat transfer rate $\dot{Q}_{\mathrm{cooling}}$ can be divided into the heat transfer rate through the insulation wall from the ambiance, $\dot{Q}_{\mathrm{ambiance}}$, and the electrically applied heating load P_{el}.

$$\dot{Q}_{\mathrm{cooling}} = \dot{Q}_{\mathrm{ambiance}} + P_{\mathrm{el}} \tag{15}$$

$\dot{Q}_{\mathrm{ambiance}}$ can be expressed in terms of the heat transmission coefficient U:

$$\dot{Q}_{\mathrm{ambiance}} = U \cdot A_{\mathrm{box}} \cdot \Delta T \tag{16}$$

where $A_{\mathrm{box}} = 2.245 \pm 0.003$ m^2 is the surface of the test box and $\Delta T = |T_{\mathrm{box}} - T_{\mathrm{ambiance}}|$. The U-value is a classification number for the insulation of the system. The smaller the U-value, the less heat transfer through the insulation occurs. From equations 15 and 16 the U-value of the test box can be calculated when $P_{\mathrm{el}} = 0$:

$$U = \frac{\dot{Q}_{\mathrm{cooling}}}{A_{\mathrm{box}} \cdot \Delta T} \tag{17}$$

The heat transfer rate $\dot{Q}_{\mathrm{cooling}}$ is plotted against the heating load P_{el} in the last plot of Fig. 34 (appendix: Fig. 41, 42, 43 and 44). A summary of the U-values can be found in Table 2. The error on ΔT is large, because the error of the temperature sensors is of the same order as the temperature difference. To calculate the empirical heat transmission coefficient from literature the following equation was applied:

$$U_{\mathrm{th}} = \frac{1}{R_{\mathrm{se}} + \frac{s_{\mathrm{AIREX}}}{\lambda_{\mathrm{AIREX}}} + \frac{s_{\mathrm{wood}}}{\lambda_{\mathrm{wood}}} + R_{\mathrm{si}}} \approx 0.73 \quad \frac{\mathrm{W}}{\mathrm{m}^2 \cdot \mathrm{K}} \qquad [17] \tag{18}$$

with $R_{\mathrm{se}} = 0.04$ (m$^2 \cdot$ K)/W the outer heat transmission resistance [17], $s_{\mathrm{AIREX}} = 0.04$ m the layer thickness of the AIREX isolation, $\lambda_{\mathrm{AIREX}} = 0.036$ W/(m·K) the thermal conductivity of the AIREX [18], $s_{\mathrm{wood}} = 0.012$ m the wall thickness of the wooden test box, $\lambda_{\mathrm{wood}} \approx 0.15$ W/(m·K) the thermal conductivity of wood [19], and $R_{\mathrm{si}} = 0.13$ (m$^2 \cdot$ K)/W the inner heat transmission resistance [17].

Due to the large uncertainties a discussion of the measured $\dot{Q}$ and U-values is difficult. Although it can be said, that the value of U in Table 2 is in fair agreement with U_{th}.

3.5.3 Influence of the flow rate on the temperatures

To get a feeling for the effect of the flow rate on the temperatures, a test series with different flow rates at maximal heating load of $P = 240$ W was done. Below $100\,\ell$/h the flow rate was increased in steps of $10\,\ell$/h and above $100\,\ell$/h in steps of $20\,\ell$/h. Figure 35 shows the temperature differences versus the flow rate. In the left plot the fast decrease in temperature for low flow rates changes into a slow decrease towards high flow rates. The middle plot shows the kink which marks the boundary between the laminar and the turbulent flow region. The right plot shows the development of the relative humidity RH and the temperature T_{box} in the test box together with the dew point. If the dew point, TP, reaches the coldest temperature in the box, condensation at this location would begin which is at the cooling pipe close to the inlet. The dew point is calculated with the following formula [8]:

$$\mathrm{TP} = \frac{241.2 \cdot \ln\frac{\mathrm{RH}}{100} + \frac{4222.03716 \cdot T_{\mathrm{box}}}{241.2 + T_{\mathrm{box}}}}{17.5043 - \ln\frac{\mathrm{RH}}{100} - \frac{17.5043 \cdot T_{\mathrm{box}}}{241.2 + T_{\mathrm{box}}}} \quad {}^{\circ}\mathrm{C} \tag{19}$$

with

$$\lim_{\mathrm{RH} \to 100} \mathrm{TP} = T_{\mathrm{box}} \tag{20}$$

and T_{box} given in units of °C. The results in the right plot of Fig. 35 show the dew point below the lowest temperature of the cooling plate and therefore no condensation is expected.

To get an estimate on how turbulent the flow rate f is, the Reynolds number Re for our tubes was calculated as

$$Re = \frac{\rho \cdot L \cdot \bar{v}}{\eta} \quad [20] \quad . \tag{21}$$

The dynamic viscosity $\eta = \nu \cdot \rho$ is replaced by the kinematic viscosity $\nu = \frac{\eta}{\rho}$ of the cooling fluid and the inner diameter of the tube L is given by $2 \cdot R$, the radius of the cooling pipe. Equation 21 becomes then:

$$Re = \frac{2 \cdot R \cdot \bar{v}}{\nu} \tag{22}$$

The mean velocity $\bar{v}$ is simply calculated by

$$\bar{v} = \frac{f}{\pi \cdot R^2} \tag{23}$$

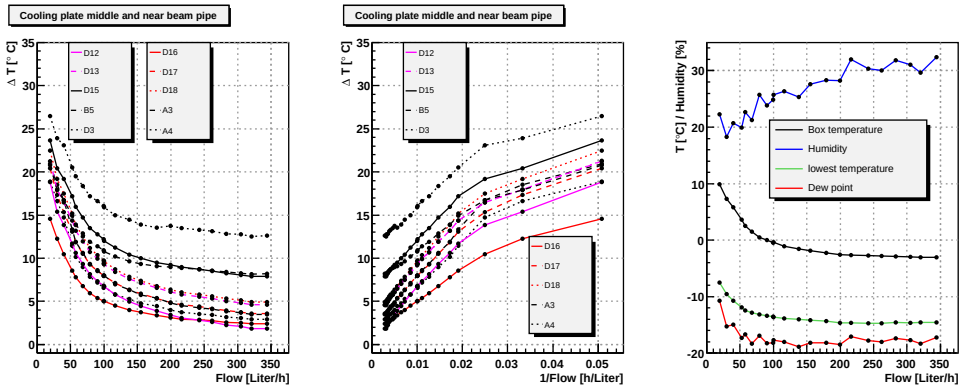

Figure 35: Results of the development of the temperatures at different flow rates. The first two frames show, that a designed flow rate of 250ℓ/h is a good choice, since the turbulent region is clearly reached and higher flow rates do not bring significant decreases of the temperatures anymore. The third plot shows, that the dew point is below the lowest temperature of the cooling plate: no condensation is expected. The measurement was done using a total dissipated heat of $P = 240$ W.

When equation 23 is inserted into equation 22 the Reynolds number is expressed as

$$Re = \frac{2 \cdot f}{\pi \cdot R \cdot \nu} \tag{24}$$

where R is the inner radius of the tube amounting to 0.004 m. The kinematic viscosity ν of the cooling fluid C_6F_{14} at $-15°$C was given with $\nu = 0.69$ centi Stokes $= 6.99 \cdot 10^{-7}$ m^2/s [21]. The critical Reynolds number Re_{crit}, characterizing the transition to the turbulent region, is $\text{Re}_{\text{crit}} \approx 2300$ for a straight, smooth tube [20]. The results in Figure 35 show the typical kink at ~ 0.024 h/$\ell \approx 42\,\ell$/h corresponding to a Reynolds number of $Re \approx 2656$. This result is in good agreement with the cited Re_{crit} from [20] and shows that a nominal flow of $250\,\ell$/h corresponding to a Reynolds number of ~ 15812 is well in the turbulent region. Figure 35 shows as well that higher flow rates than $250\,\ell$/h do not much improve the temperature behavior. A nominal flow of $250\,\ell$/h is a safe and economic solution.

4 Thermal characterization of the TT-station

As a cooling test of the whole system, the complete TT station was cooled while simulating the full heat load of the beetles through Kapton heating elements as in chapter 3. The following studies were made:

- Temperature profile at different heating loads,
- U-value of the TT station box,
- Temperature profile at warm up.

4.1 Experimental setup

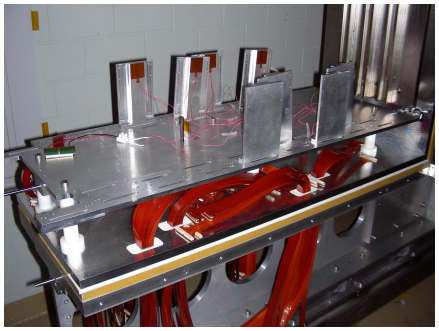

Figure 36: Cooling plate equipped with 8 balconies carrying Kapton heaters, which were serially connected to a power supply.

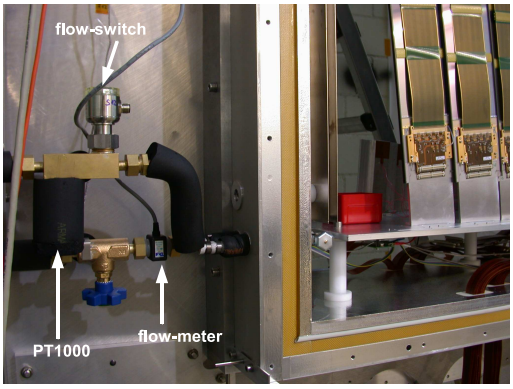

Figure 37: Cooling supply and return lines at the exit of one cooling plate. The flow-meter is in the supply line, the flow-switch and the PT1000 are in the return line. The PT1000 is covered with black thermal isolation.

The full station was built in the assembly hall 36G38 in Zürich as a test for the assembly at CERN. The cooling system had to be connected to the side plates and the balcony cooling plates. Several isolated tubes led from the station to the same chiller which was used for the thermal studies with the test box (chapter 3). All four cooling plates were installed at the station and each of them was equipped with 8 balconies. As in the test box, Kapton heaters were glued to the balconies (Fig. 36). All the box covers and the beam pipe isolation were attached, providing a closed volume for the thermal studies. The volume cooling (side plates) and the cooling plates were populated with temperature sensors of type A and C and humidity sensors (see chapter 3). To monitor the air temperature near the beam pipe, temperature sensors A23 and A24 were hanging in the vicinity of the beam pipe. The supply lines of the cooling fluid have one PT1000 at each side to monitor

the ingoing temperature and each branch to the cooling or side plates was equipped with its own flow-meter (IR-Opflow). The return lines of the cooling plates and side plates were connected to a flow-switch FS10 and a PT1000. The sensors PT1 to PT12 are of type B integrated in a tube sitting directly in the fluid (see Figure 37). For an exact overview of the experimental setup and the positioning of the temperature sensors see Fig. 38. Dry air was purged through the cooled volume to prevent condensation.

4.2 Data reconstruction

The data reconstruction was very comparable to the one used for the test box (chapter 3.2). The only difference was that all ports of the data acquisition board were occupied by serial cables. In addition, all the PT1000 located in the fluid (outside of the box) were connected to the serial cables via a separate patch panel on the magnet side of the C-frame. The data acquisition board was able to read out at most 3 pairs of serial cables in parallel. Therefore one test series for the full station comprised again 2 different configurations: the outer patch panel on both sides on top of the station plus one of the patch panels on the C-frame, or the outside patch panel on both sides at the bottom of the station with one patch panel on the C-frame. All sensors were plugged at the same position in all measurements. The readout device for the flow-meters was designed and assembled by Prof. Dr. U. Straumann. However, the flow rate was not monitored continously by a computer. Instead it was only regulated at the beginning of a test series.

4.3 Calibration

The same type of calibration as in chapter 3.3 was done for all water proof sensors in the station. The results can be found in Table 9 in the appendix. Differences in the offsets were observed between type A, type PT elevator side and type PT cryo side. Therefore PT1 was calibrated with the mean offset of PT2 to PT6 of 0.458, and PT12 was calibrated with the mean offset of PT7 to PT11 of 0.646. The effect of the average slope of $s = 0.974$ on the measured temperatures is smaller than the measuring uncertainty of the temperatures, therefore the slope was not corrected ($s = 1$). The sensors of type C could not be calibrated with water, therefore the slope $s = 0.974$ was assumed to be the mean of the other sensors and the offsets O_{C} were calculated using the measured value at room temperature $T_{\mathrm{room}} = 23°\mathrm{C}$.

$$O_{\mathrm{C}} = T_{\mathrm{C}} - s \cdot T_{room} \tag{25}$$

The values for T_{room} and the offset can be seen in table 10 in the appendix. Unfortunately, C1 and C2 were not individually calibrated and therefore the offset of the corresponding sensor at the other detector side was simply taken ($O_{\mathrm{C1}} = O_{\mathrm{C5}}$, $O_{\mathrm{C2}} = O_{\mathrm{C6}}$).

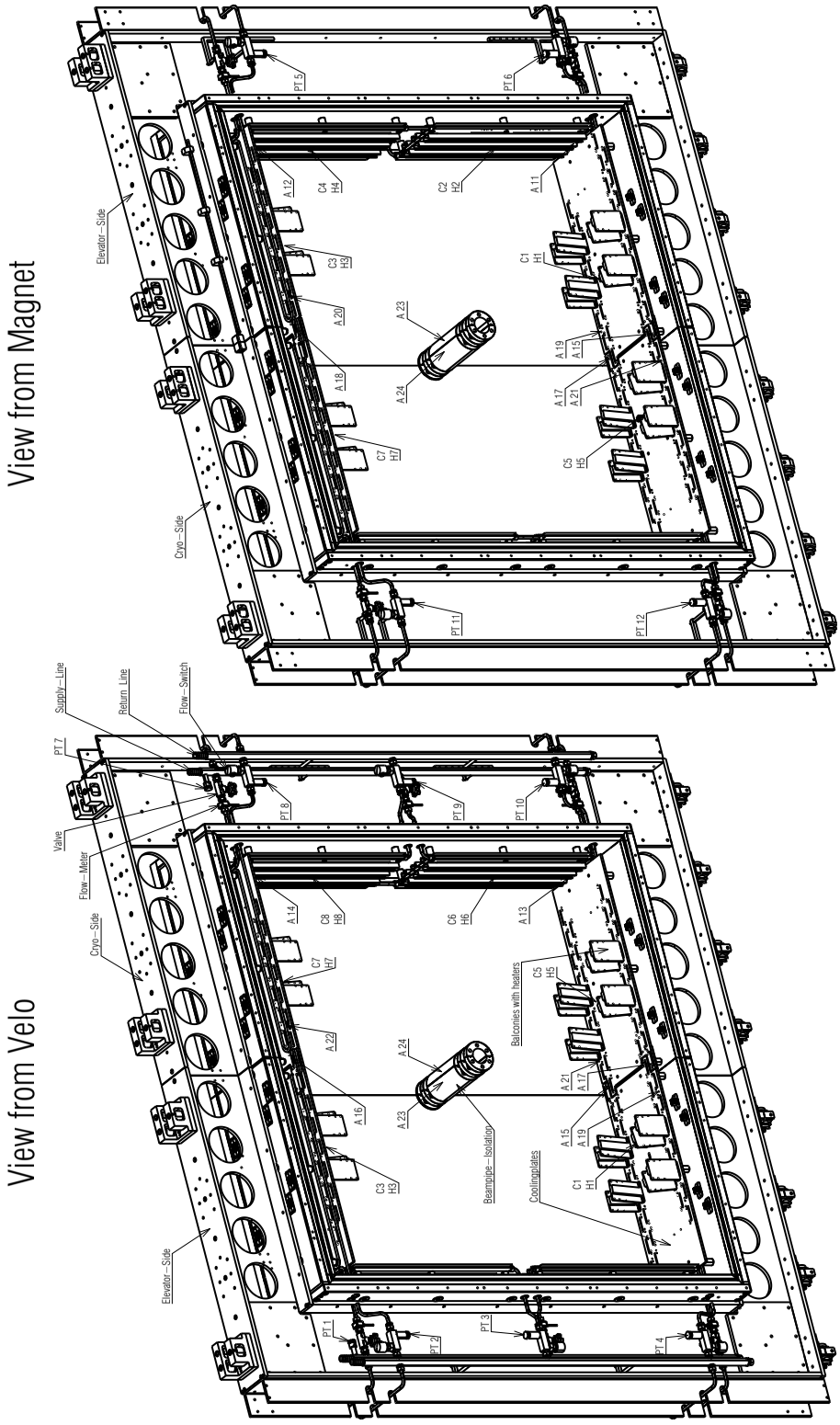

Figure 38: Detailed plan of the temperature sensor locations and the experimental setup.

4.4 Temperature profile for heating load measurements

A similar heating load test series was performed as in chapter 3.5.1. The nominal temperature of the cooling fluid C_6F_{14} was set to $-15°C$. The flow rates were adjusted individually for each cooling cycle. For the volume cooling (side plates) it was set to $200\,\ell$/h. It appeared that the chiller already reached its maximum pumping capacity with flow rates through each of the cooling plates between 180-$210\,\ell$/h. For the cooling plates on the elevator side, which was further away from the chiller, the flow rates reached $\sim 190\,\ell$/h while on the cryo side the flow rates reached $\sim 220\,\ell$/h. So, for the cooling plates the maximum possible flow rate was used. Each half of the station had its own power supply for the heaters.

The estimated heating load of one beetle is ≤ 0.8 W and the full station holds 1120 beetles. Therefore the total expected heating load is ≤ 896 W. A test series started with a measurement without any heating load ($P = 0$). Then measurements were taken with the power P increased in steps of 200 W to 1200 W, i.e. $\sim 30\%$ more than the total expected heating load at the station. After increasing the power, the thermal equilibrium was reached in about half an hour, as for the test box.

Figure 39 shows the temperatures in the station from the heating load measurement. The colors indicate sensors of the same quadrant. Interestingly, the temperatures of the upper cooling plates (green and red colored) were cooler than the corresponding lower ones. A possible explanation might be the distribution lines of the cooling fluid, since the distribution went from up to down such that the cooling fluid was already warmed up a bit before it reached the lower cooling plates. The opposite effect was observed for the air temperatures inside the box: the temperatures of the upper sensors (C3 and C7) were higher than the ones in the center (A23 and A24) and those were warmer than the lower ones (C1 and C5). Sensors screwed to a cooling- or side plate had a maximal temperature of $-12°C$ as the first three plots show in Fig 39. The sensors of the inlets PT1 and PT7 gave the coldest temperature readings. At the nominal heating load of 900 W the warmest measured temperature in the station was $\sim -3°C$. Increasing the heating load to a maximum of 1200 W for the station, the warmest temperature was $\sim -1.2°C$. In conclusion the cooling tests showed that the station can be maintained well below $0°C$ which is a very promising result and provides in addition some margin with respect to the design value for operation of $5°C$.

4.5 U-value of the station box

Similar to the determination of the U-value from chapter 3.5.2 the same procedure was repeated for the station. Since the flow rate was adjusted for each cooling circuit individually, the $\dot{Q}$ value was calculated for each circuit and summed to determine the total heat transfer rate:

$$\dot{Q}_{\text{cooling}} = \sum_{i=1}^{10} \dot{Q}_{\text{i}} \tag{26}$$

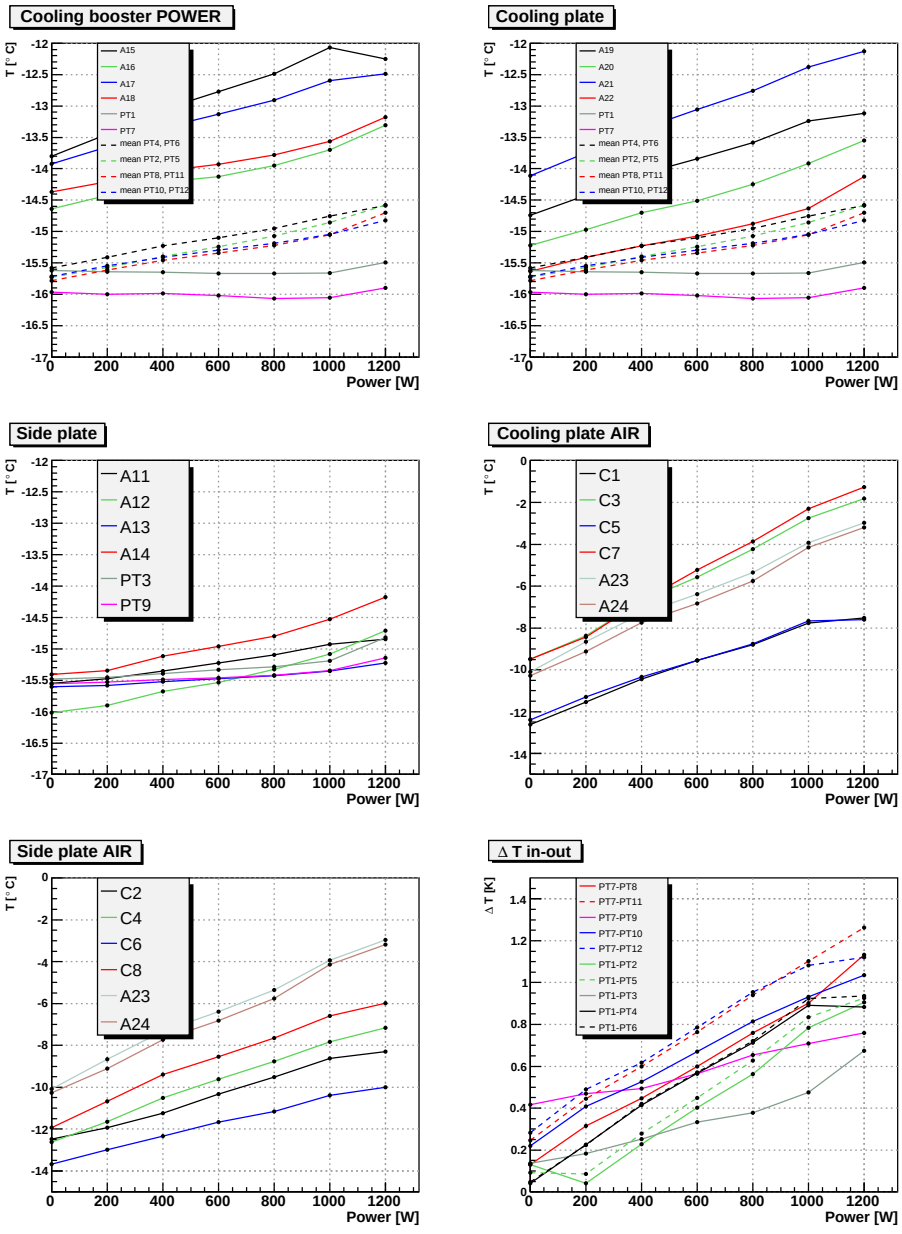

Figure 39: The temperature and temperature difference of the sensors versus the heating power. The colors indicate sensors of the same quadrant: cryo up is red, elevator up is green, cryo down is blue and elevator down is black.

where $\dot{Q}_i$ are the heat transfer rates of the individual cooling circuits:

$$\dot{Q}_i = C_i \cdot \rho_i \cdot f_i \cdot (T_i^{\text{in}} - T_i^{\text{out}}) \tag{27}$$

ρ_i and C_i are calculated from equations 13 and 14 on page 29. The U-value is then obtained:

$$U_{meas} = \frac{\dot{Q}_{\text{cooling}}}{A_{\text{TTbox}} \cdot \Delta T} = 0.55 \pm 0.32 \quad \frac{\text{W}}{\text{m}^2 \cdot \text{K}} \tag{28}$$

where $A_{\text{TTbox}} = 10.677$ m^2 is the surface of the TT station box and $\Delta T = |T_{\text{TTbox}} - T_{\text{room}}|$ where T_{room} is the room temperature in the experimental hall and T_{TTbox} the average temperatures of the sensors C1 to C8, A23 and A24 inside the box. Due to the large errors on $T_i^{\text{in}} - T_i^{\text{out}}$ and on the the flow rates f_i the uncertainty on $\dot{Q}$ and U is also large. The errors of ρ_i and C_i were neglected and the error of the flow rate was estimated to be 10%, taking into account a steady decrease of the flow rate over the data taking period.

Based on empirical considerations U_{th} can be calculated by:

$$U_{\text{th}} = \frac{1}{R_{\text{se}} + \frac{s_{\text{AIREX}}}{\lambda_{\text{AIREX}}} + \frac{s_{\text{Al}}}{\lambda_{\text{Al}}} + \frac{s_{\text{kevlar}}}{\lambda_{\text{kevlar}}} + R_{\text{si}}} = 0.77 \quad \frac{\text{W}}{\text{m}^2 \cdot \text{K}} \qquad [17] \tag{29}$$

with $R_{\text{se}} = 0.04$ (m$^2\cdot$ K)/W the outer heat transmission resistance [17], $s_{\text{AIREX}} = 0.04$ m the layer thickness of the AIREX isolation, $\lambda_{\text{AIREX}} = 0.036$ W/(m·K) the thermal conductivity of the AIREX [18], $s_{\text{Al}} = 2 \cdot 25 \cdot 10^{-6}$ m the thickness of the aluminium layer, $\lambda_{\text{Al}} = 209$ W/(m·K) [19], $s_{\text{kevlar}} = 2 \cdot 3 \cdot 10^{-4}$ m the thickness of the kevlar layer, $\lambda_{\text{kevlar}} = 0.04$ W/(m·K) [22] and $R_{\text{si}} = 0.13$ (m^2·K)/W the inner heat transmission resistance [17].

U_{th} and U_{meas} are consistent with each other. Compared to the previously determined U-value from the test box in chapter 3 the station box turned out to be better insulated. For future studies of the U-value a reduction of the uncertainties on $T_i^{\text{in}} - T_i^{\text{out}}$ and on flow rate is recommended.

4.6 Warm up measurement

After the cooling measurements, the chiller and the heaters were switched off and the station warmed up to room temperature. To register this warming-up a temperature measurement was taken every ~ 30 min. A typical function for warm-up processes is given by [13]:

$$T(t) = T_0 - (1 - e^{-\kappa \cdot t}) \cdot (T_0 - T_{\text{room}}) \tag{30}$$

with $T(t)$ the temperature of a sensor in the station at a given time t, T_0 the initial temperature of the station at the beginning of the test series, κ a thermal parameter which is discussed later and T_{room} the room temperature of the experimental hall. The constraints at $t = 0$ and $t = \infty$ are:

$$\lim_{t \to 0} T(t) = T_0 \qquad \text{and} \qquad \lim_{t \to \infty} T(t) = T_{\text{room}} \tag{31}$$

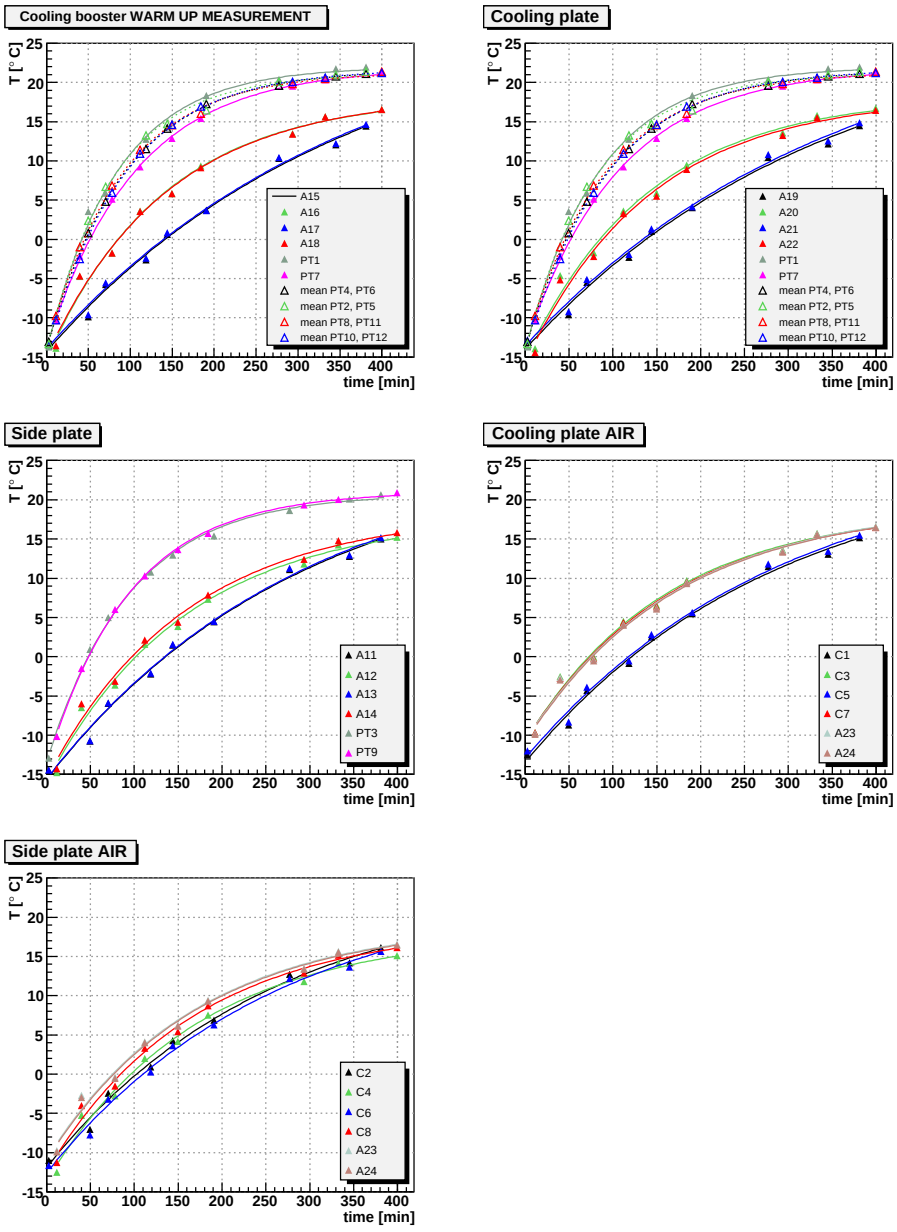

Figure 40: Results of the warm-up measurement for the full station. The fit describes the data well. After roughly 6 h 40 min (400 min) the station reached room temperature.

Figure 40 shows the data together with the fit of the parameters κ, T_0 and T_{room}. The fitted function is in good agreement with the data points. This test series demonstrated that a complete warm-up of the station from $T_0 \approx -12°\mathrm{C}$ will take more than 6 h to a room temperature of $\sim 23°\mathrm{C}$.

The thermal parameter κ is proportional to the surface of the insulating walls times the heat transmission coefficient U and inverse proportional to the cold mass of the air inside the box, m_{air} and its specific heat capacity $c_{\mathrm{v,air}}$. A large value of κ corresponds then to a fast warming up process of the thermal body. Out of the fitted parameter κ the U-value is calculated for comparison with U_{meas} from chapter 4.5.

$$U_{\mathrm{warm-up}} = \frac{\kappa \cdot c_{\mathrm{v,air}} \cdot m_{\mathrm{air}}}{A_{\mathrm{TTbox}}} = 0.84 \quad \frac{\mathrm{W}}{\mathrm{m}^2 \cdot \mathrm{K}} \tag{32}$$

where $A_{\mathrm{TTbox}} = 10.677\ \mathrm{m}^2$ is the surface of the TT station box, $c_{\mathrm{v,air}} = 1005\,\mathrm{J}/(\mathrm{K} \cdot \mathrm{kg})$ is the specific heat of air at 5°C[3] and $m_{\mathrm{air}} = 1.740$ kg the mass of air. $U_{\mathrm{warm-up}}$ is close to $U_{\mathrm{meas}} = 0.55 \pm 0.32 \frac{\mathrm{W}}{\mathrm{m}^2 \cdot \mathrm{K}}$ and $U_{\mathrm{th}} = 0.77 \frac{\mathrm{W}}{\mathrm{m}^2 \cdot \mathrm{K}}$.

This demonstrates how well the temperature performance of the detector station can be modeled as a thermal system parameterized by a few numbers only.

[3] which is approximately the average between $-15°$ and $23°\mathrm{C}$

5 Conclusions

The lower rails of the TT station were adjusted with a very high precision of ± 0.1 mm in height as well as in the horizontal plane over the entire 8 m length. We managed to align the upper rails within 1.17 mm for the height and less than 1 mm horizontally. Since the upper rails merely have a guiding function, a larger deviation is still acceptable.

The cooling tests in the test box were very successful and gave a solid base to estimate the final temperature in the station and the heat transmission coefficient U. The cooling of the full station was equally successful with a temperature below 0° C with a dissipated heat 30% above the maximum expected heating load from the beetles. With the expected heating load of 900 W the station did not get warmer than -3°C and no condensation was observed. In the operation of the TT station the warmest location at the cooling plate is at the center. The measurements revealed the need for an improvement at the cooling plates which was successfully implemented. The measured U-value amounts to $0.55 \pm 0.32 \, \frac{\mathrm{W}}{\mathrm{m}^2 \cdot \mathrm{K}}$ which is of the same order of magnitude as the measured U-values of the test box (between 1.05 $\frac{\mathrm{W}}{\mathrm{m}^2 \cdot \mathrm{K}}$ and 2.42$\frac{\mathrm{W}}{\mathrm{m}^2 \cdot \mathrm{K}}$) and the U_{th} from literature (0.73 $\frac{\mathrm{W}}{\mathrm{m}^2 \cdot \mathrm{K}}$ for the test box and 0.77 $\frac{\mathrm{W}}{\mathrm{m}^2 \cdot \mathrm{K}}$ for the full station). The complete warm-up of the station took about 6 h for a room temperature of about 23° C.

6 Acknowledgments

Special thanks go to Prof. Dr. Ulrich Straumann for the opportunity to join his group and for his credit to commit a master-thesis to me with hand work on the detector. I also appreciate his understanding of supervision: as support with helpful discussions whenever problems arose, be it with Reynolds numbers or the ROOT software. I want to express my gratitude to my supervisor Frank Lehner for all the hours at the phone, helping me with the interpretation of the results and with his immense knowledge about our detector. I appreciate very much his careful correction of my thesis with so many valuable hints. Many thanks go to Stefan Steiner for anticipating my every wish for a technical drawing and for all technical input, the discussion and correction of the thesis. Also for the pleasant collaboration in the assembling of the station and the company in the evenings at Geneva. I want to mention the team of the workshop with Kurt Bösiger, for all the expert advice and their commitment to finish last minute modifications or rearrangements just in time, so the tight schedule could be met. Jeroen van Tilburg might bore the biggest brunt of work for correction. I thank him so much for all the input as well as for inspiring discussions and for the enjoyable collaboration, be it down in the pit or in meetings. I also estimate the support of Achim Vollhardt during the measurements, helping me out when ever an electronically related problem occurred. I want to thank my husband Andi who plunged for a while in the world of a particle physicist while correcting my thesis. Many thanks go to the whole LHCb team of the University of Zürich for their encouraging company.

References

[1] Prof. Dr. Ulrich Straumann, Physics Institute of the University of Zürich, Forschungsgesuch Nationalfonds HERA/LHCb, *Research plan for LHCb*, September 2006

[2] LHCb Outer Tracker Home Page, *http://www.nikhef.nl/pub/experiments/bfys/lhcb/outerTracker/images/LHCb-Tracking.jpg*, (19th of January 2007)

[3] LHCb Silicon Tracker - Material for Publications, *http://www.physik.unizh.ch/groups/lhcb/public/material/index.php*, (19th of January 2007)

[4] The LHCb Collaboration, *LHCb Technical Design Report, Reoptimized Detector Design and Performance*, CERN Geneva, 2003; ISBN: 92-9083-209-6

[5] LHCb Note 2006-063, *Design and Production of Detector Modules for the LHCb Silicon Tracker*, 29th of November 2006

[6] André Froton TS/SU, Jean-Christophe Gayde TS/SU, *LHCb - Trigger Tracker position of rail top supports after adjustment references for rails adjustment*, EDMS document ID 761225, CERN, Week 30, 2006

[7] Stefan Steiner, Physics Institute of the University of Zürich, *Technical drawings by CATIA V.5*, January 2007

[8] Ueli Bieler, *Praktikumsbericht*, 9th of May, 2006

[9] Wheatstone Messbrücke, *http://www.elektronik-kompendium.de/sites/slt/0306151.htm*, (15th of January 2007)

[10] Data sheet 90.6125, JUMO GmbH & Co. KG, *Platinum-chip temperature sensors in SMD style to EN 60 751*, October 2006

[11] Tolerance classes, IST AG, *http://www.ist-ag.com/english/products/temp/platin.html*, (16th of January 2007)

[12] Applications Note 2005.1 Rev A, Hygrometrix Inc., *Basic Signal Conditioning for the HMX2000-HT Hygro-thermal Sensor*, May 2005

[13] PD Dr. Frank Lehner, Physics Institute of the University of Zürich, private communication

[14] Michael Dimmler, KME Zürich, *Maturitätsarbeit*, January 2006

[15] Specifications of the IR-Opflow turbine flowmeter, Tecflow Interational, *http://www.tecflow.nl/technical_page_brochure.pdf*, (13th of February 2007)

[16] Product Information, 3M Electronics Markets Materials Division, *3M Performance Fluid PF*5060, November 2003

[17] Wärmedurchgangskoeffizient, wikipedia, *http://de.wikipedia.org/wiki/Thermische_Leitf%C3%A4higkeit*, (15th of January 2007)

[18] Data sheet, Alcan Airex AG, *AIREX® R82 high performance foam*, October 2005

[19] Wärmeleitfähigkeit, wikipedia, *http://de.wikipedia.org/wiki/W%C3%A4rmeleitkoeffizient*, (31th of January 2007)

[20] Roland Engfer, Physics Institute of the University of Zürich, *Physik A I für Naturwissenschaftler*, August 2002

[21] C_6F_{14} Properties, CERN, *http://st-support-cooling-electronics.web.cern.ch/st-support-cooling-electronics/CWGWeb/C6F14Prop.htm*, (14th of February 2007)

[22] Wärmeleitfähigkeit, GoodFellow, *http://www.goodfellow.com/csp/active/STATIC/G/Polyaramid.HTML*, (31th of January 2007)

[23] Spezifische Wärmekapazität, wikipedia, *http://de.wikipedia.org/wiki/Spezifische_W%C3%A4rmekapazit%C3%A4t*, (31th of January 2007)

[24] Luftdichte, wikipedia, *http://de.wikipedia.org/wiki/Dichte_der_Luft*, (31th of January 2007)

A Alignment data tables

Table 3: Data of final leveling of the lower rails

$y_{rel} \pm 15$ [mm]	i $\pm$ 0.1 [1/10 mm]	d$_Z$ $\pm$ 0.01 [mm]
1100	54.0	0.10
1700	54.1	0.09
2300	54.1	0.09
2600	54.1	0.09
2900	54.0	0.10
3200	54.0	0.10
3500	54.0	0.10
3800	54.0	0.10
3950	54.1	0.09
4250	54.1	0.09
4550	54.1	0.09
4850	54.1	0.09
5150	54.4	0.06
5450	54.7	0.03
6050	54.8	0.02
6650	54.5	0.05

Table 4: Data of final leveling of the upper rails

$y_{rel} \pm 15$ [mm]	i $\pm$ 0.1 [1/10 mm]	$d_Z \pm 0.01$ [mm]
50	63.1	-0.81
200	64.0	-0.90
500	59.8	-0.48
800	57.1	-0.21
1100	55.5	-0.05
1400	54.2	0.08
1700	53.5	0.15
2000	53.0	0.20
2300	53.0	0.20
2600	53.6	0.14
2900	54.8	0.02
3200	57.2	-0.22
3500	60.5	-0.55
3800	63.9	-0.89
3950	63.2	-0.82
4250	63.0	-0.80
4550	63.0	-0.80
4850	63.0	-0.80
5150	64.0	-0.90
5450	64.1	-0.91
5750	64.4	-0.94
6050	64.5	-0.95
6350	64.3	-0.93
6650	64.0	-0.90
6950	63.8	-0.88
7250	62.9	-0.79
7550	62.1	-0.71
7700	62.2	-0.72

Table 5: Data of final x-alignment of the upper rails with the theodolite

y_{rel} ± 15 [mm]	ruler [mm]	$\mathrm{d_{Xup}}$ [mm]
50	148.1 ± 0.30	0.66 ± 0.30
200	148.1 ± 0.30	0.66 ± 0.30
500	148.1 ± 0.29	0.66 ± 0.29
800	148.1 ± 0.28	0.66 ± 0.28
1100	148.1 ± 0.27	0.61 ± 0.27
1400	148.1 ± 0.26	0.61 ± 0.26
1700	147.9 ± 0.26	0.51 ± 0.26
2000	147.9 ± 0.25	0.51 ± 0.25
2300	147.9 ± 0.24	0.51 ± 0.24
2600	147.9 ± 0.23	0.51 ± 0.23
2900	148.0 ± 0.23	0.56 ± 0.23
3200	147.9 ± 0.22	0.51 ± 0.22
3500	148.0 ± 0.21	0.56 ± 0.21
3800	148.0 ± 0.20	0.56 ± 0.20
3950	147.9 ± 0.20	0.46 ± 0.20
4250	147.9 ± 0.19	0.51 ± 0.19
4550	147.9 ± 0.18	0.51 ± 0.18
4850	148.0 ± 0.17	0.56 ± 0.17
5150	148.0 ± 0.17	0.56 ± 0.17
5450	148.0 ± 0.16	0.56 ± 0.16
5750	148.0 ± 0.15	0.56 ± 0.15
6050	148.1 ± 0.14	0.61 ± 0.14
6350	148.1 ± 0.14	0.61 ± 0.14
6650	148.1 ± 0.13	0.61 ± 0.13
6950	148.1 ± 0.12	0.61 ± 0.12
7250	148.1 ± 0.11	0.61 ± 0.11
7550	148.1 ± 0.10	0.66 ± 0.10
7700	148.1 ± 0.10	0.66 ± 0.10

Table 6: Data of the x-alignment of the lower rails with the theodolite

y_{rel} ± 15 [mm]	ruler [mm]	$\mathrm{d_{Xdown}}$ [mm]
1100	138.5 ± 0.27	0.51 ± 0.27
1400	138.5 ± 0.26	0.51 ± 0.26
1700	138.5 ± 0.26	0.51 ± 0.26
2600	138.4 ± 0.23	0.46 ± 0.23
2900	138.5 ± 0.23	0.51 ± 0.23
3200	138.4 ± 0.22	0.46 ± 0.22
3500	138.5 ± 0.21	0.51 ± 0.21
3800	138.5 ± 0.20	0.51 ± 0.20
3950	138.4 ± 0.20	0.46 ± 0.20
4250	138.4 ± 0.19	0.46 ± 0.19
4550	138.4 ± 0.18	0.41 ± 0.18
4850	138.5 ± 0.17	0.51 ± 0.17
5150	138.5 ± 0.17	0.51 ± 0.17
5450	138.6 ± 0.16	0.56 ± 0.16
6050	138.5 ± 0.14	0.51 ± 0.14
6650	138.5 ± 0.13	0.51 ± 0.13

Table 7: Data of the x-alignment of the lower rails with the laser

$y_{rel} \pm 15$ [mm]	$\mathrm{d_{Xlaser}} \pm 0.02$ [mm]
1100	-0.008
1400	-0.013
1700	-0.016
2000	-0.041
2300	-0.044
2600	-0.071
2900	-0.083
3200	-0.084
3500	-0.069
3800	-0.040
3950	-0.065
4250	-0.090
4550	-0.077
4850	-0.053
5150	-0.057
5450	-0.056
5750	-0.034
6050	-0.031
6350	0.028
6650	0.041

B Calibration data tables

Table 8: Calibration for 32 out of 46 test box sensors

sensor	T @ 0°C	T @ 22.5°C	slope	offset
A2	1.92	24.92	1.0221	1.92
A3	2.42	25.5	1.0258	2.42
A4	2.38	25.41	1.0231	2.38
A5	2.55	25.63	1.0258	2.55
A6	2.18	25.22	1.0240	2.18
A7	2.22	25.25	1.0234	2.22
D4	2.12	25.36	1.0332	2.12
B4	2.09	25.07	1.0211	2.09
D5	1.99	25.19	1.0313	1.99
A9	2.33	25.32	1.0219	2.33
A10	1.92	25.08	1.0296	1.92
B1	2.42	25.44	1.0230	2.42
D1	2.69	25.97	1.0348	2.69
D2	2.23	25.54	1.0356	2.23
D3	2.54	25.66	1.0280	2.54
D7	1.72	24.68	1.0204	1.72
D8	2.51	25.29	1.0123	2.51
D9	2.34	25.1	1.0113	2.34
D10	2.13	25.03	1.0178	2.13
D11	2.32	25.35	1.0233	2.32
D12	2.32	25.21	1.0176	2.32
D18	1.91	24.78	1.0164	1.91
D19	2.13	25.01	1.0167	2.13
D20	2.27	25.34	1.0254	2.27
D14	2.41	25.46	1.0243	2.41
D15	1.63	24.64	1.0230	1.63
D16	2.12	25.18	1.0250	2.12
D17	1.86	24.84	1.0215	1.86
E6	2.8	25.75	1.0198	2.8
E2	1.09	23.87	1.0126	1.09
E3	2.67	25.43	1.0113	2.67
E4	3.11	25.87	1.0116	3.11

Table 9: Calibration for 24 out of 34 sensors of the full station

sensor	T @ 0°C	T @ 23°C	slope	offset
A13	3.43	25.64	0.97	3.43
A17	3.24	25.49	0.97	3.24
A21	3.21	25.49	0.97	3.21
A24	3.73	26.08	0.97	3.73
A14	3.65	26.20	0.98	3.65
A18	3.70	26.12	0.97	3.70
A22	3.52	25.95	0.98	3.52
A11	3.31	25.60	0.97	3.31
A15	3.36	25.53	0.96	3.36
A19	2.87	25.11	0.97	2.87
A12	4.04	26.02	0.96	4.04
A16	2.83	25.24	0.97	2.83
A20	3.33	25.91	0.98	3.33
A23	3.21	25.70	0.98	3.21
PT7	0.56	23.32	0.99	0.56
PT8	0.54	23.07	0.98	0.54
PT9	0.84	23.40	0.98	0.84
PT10	0.52	23.06	0.98	0.52
PT11	0.77	23.53	0.99	0.77
PT5	0.43	22.90	0.98	0.43
PT3	0.56	22.90	0.97	0.56
PT2	0.47	22.81	0.97	0.47
PT6	0.31	22.74	0.97	0.31
PT4	0.52	22.78	0.97	0.52

Table 10: Calibration for the type C sensors of the full station

sensor	T_{room} in °C	offset
C1	-	3.428
C2	-	2.998
C3	26.21	3.808
C4	25.99	3.588
C5	25.83	3.428
C6	25.40	2.998
C7	26.00	3.598
C8	26.37	3.968

C Results of the heating load measurements

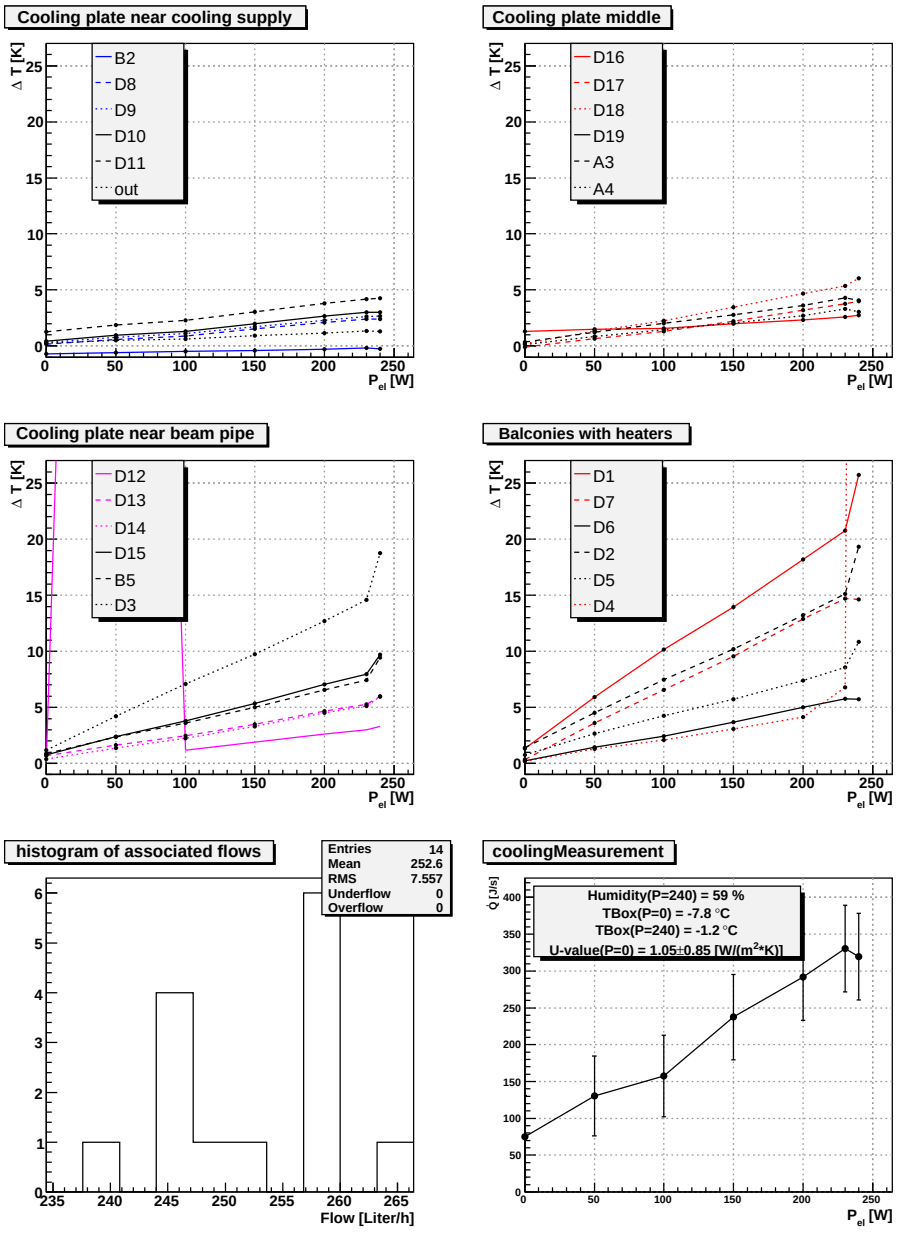

Figure 41: Plotted results of the cooling measurement.

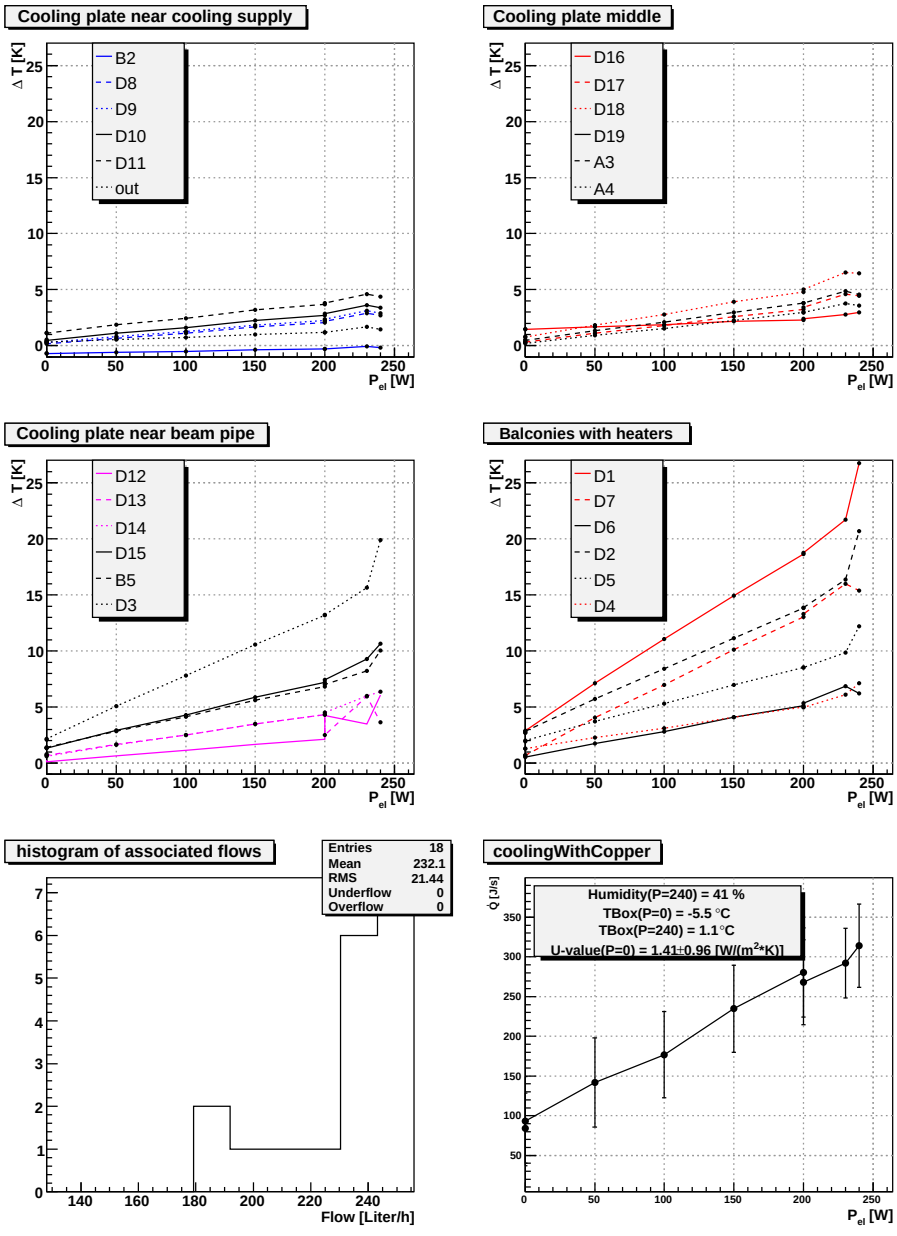

Figure 42: Plotted results of the cooling with copper measurement.

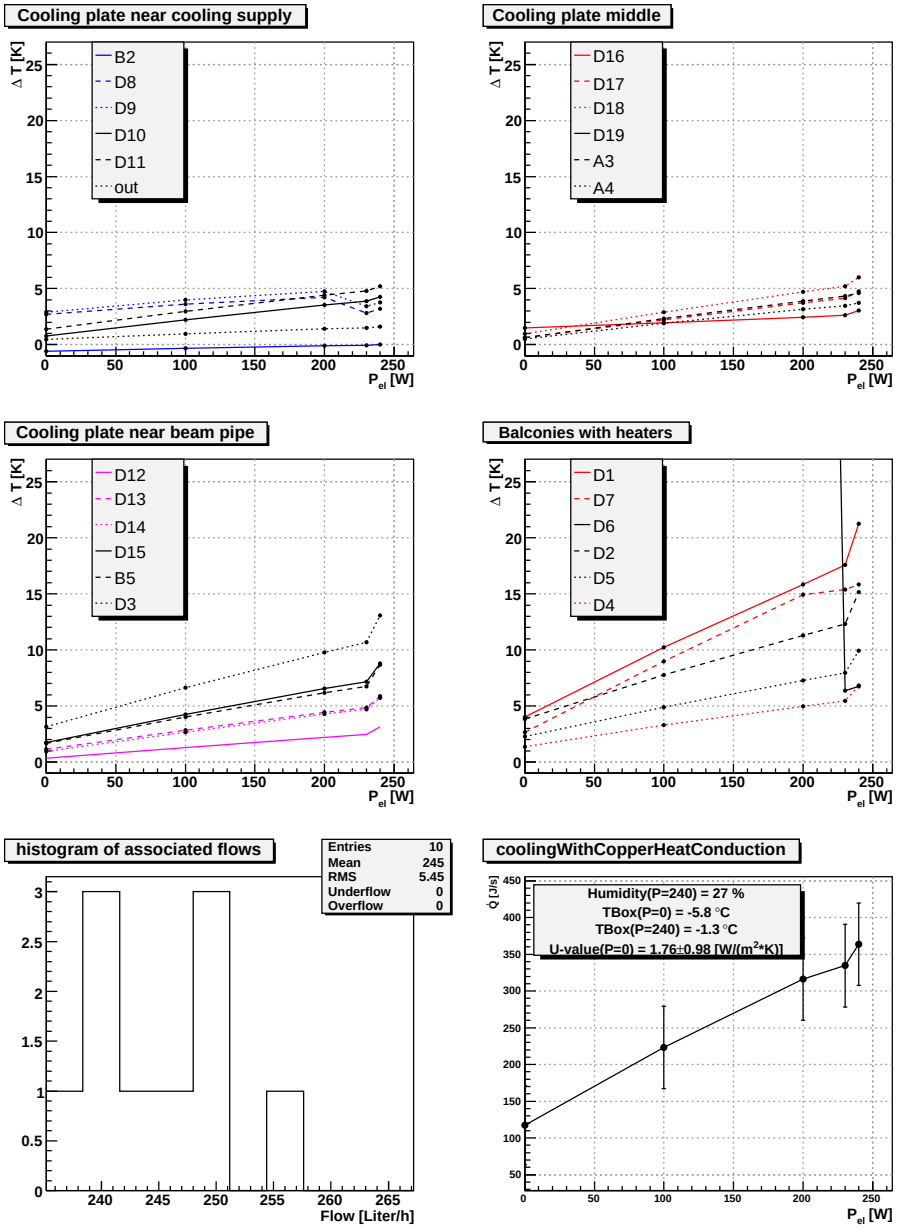

Figure 43: Plotted results of the cooling with copper and heat conduction measurement.

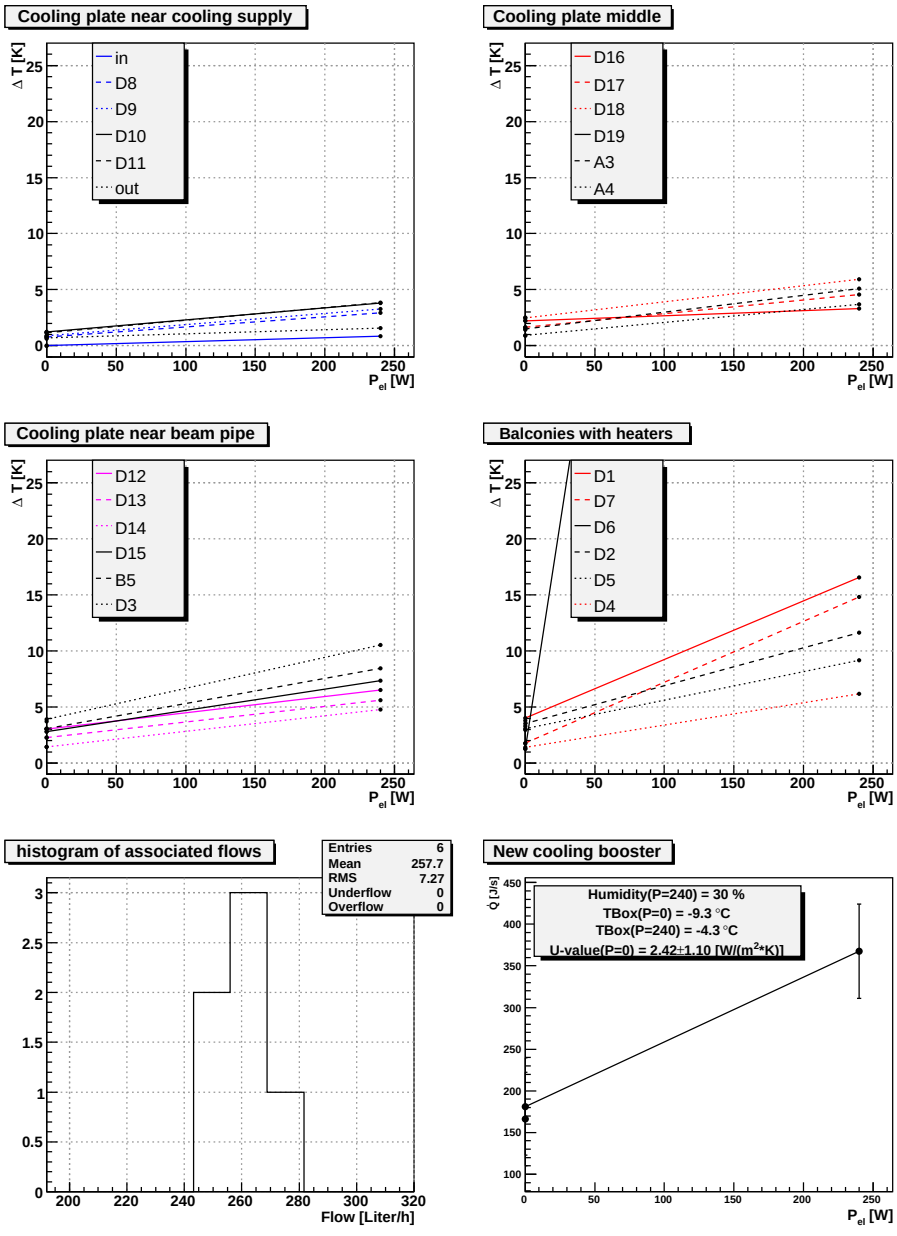

Figure 44: Plotted results of the new cooling booster measurement.

D Measurement reports